The Ordinal Dynamics of Turbulence

Permutation Entropy and Complexity in Turbulent Plasmas

Peter J Weck
Adviser: Michael Brown
Swarthmore College

March 26, 2015

Contents

1 Introduction

At the heart of turbulence physics is the idea that some flows can be made sense of only statistically, and that once we adopt a statistical perspective, universalities and symmetries begin to emerge from the chaos. Usually such statistical characteristics are identified using frequency spectra or probability distributions describing the size of fluctuations in the system across different time or length scales. However, the inherently probabilistic component to the study of turbulence also makes it amenable to more elaborate statistical measures of information and complexity. While more difficult to interpret than frequency spectra, such metrics provide a promising new way to look at turbulence, especially turbulence in plasmas where the electromagnetic character of flows contributes additional structure. In this thesis, statistical metrics known as permutation entropy and Jensen-Shannon complexity will be applied to datasets describing turbulent fluctuations in several laboratory and astrophysical plasmas. These metrics decompose a time series generated by discrete measurements of some physical parameter into ordinal patterns, similarly to how Fourier analysis decomposes a waveform into sinusoidal modes. By studying ordinal dynamics, or patterns in the relative sizes of successive values in a time series, essential information about the statistical nature of the fluctuations can be obtained. The work presented here and in [1] represents the first application of complexity and entropy measures based on ordinal patterns to astrophysical plasma turbulence or the comparison of different turbulent plasma sources. These methods have been used in other recent plasma turbulence research [2, 3], although these applications of permutation entropy and complexity were limited to a particular laboratory device at the University of California Los Angeles. The results presented in this thesis highlight important differences between the various turbulent plasmas studied, demonstrating that different types of plasma exhibit turbulent fluctuations of different statistical character, with the well-developed turbulence of the solar wind more random and less complex than in many laboratory plasmas. Thus measures of entropy and complexity could help to characterize the effectiveness of laboratory plasmas as models for astrophysical turbulence. The permutation entropy and complexity of a given turbulent plasma are shown to depend on the timescale at which the turbulence is considered, and could potentially be used to identify timescales of physical interest without prior knowledge of the system in question. Several practical conclusions, connected to the effects of insufficient statistics on these metrics, the appropriate choice of parameters, and even issues of terminology in turbulence physics are also made. On the whole, permutation entropy and Jensen-Shannon complexity constitute

promising new tools for the statistical study of turbulent fluctuations.

2 Turbulence Background

In fluid mechanics, turbulence refers to fluid motions which are so irregular that they warrant only a statistical description. In the late 1800s, it was observed that for a given geometry the transition to turbulent flow occurred at a specific value of the dimensionless control parameter

$$R = \frac{LV}{\nu}, \tag{1}$$

where ν is the viscosity, L is the characteristic scale, and V the characteristic velocity of the flow [4]. This parameter is known as the Reynolds number, and can also be interpreted as the ratio of the convective and dissipative energies of the flow. As the convective energy comes to dominate dissipation effects, perturbations on small scales are magnified and manifest themselves as highly unpredictable large scale fluctuations. In the process, symmetries present in the smooth, or laminar, flow of the fluid are broken. However, at very high Reynolds numbers, certain symmetries are said to be restored, in so far as they hold in a statistical sense far from the system's boundaries. This too was observed as early as the 1880s, when Lord Kelvin noted that a high speed fluid flow through a lattice structure appears to be statistically homogeneous and isotropic if observed far enough past the lattice [5].

Unless qualified with a particular spatial direction, to say a flow is statistically homogeneous is to say that its time-averaged values are independent of position in each of the three mutually perpendicular coordinate directions. Similarly, a statistically isotropic flow has mean values which are independent of direction. In other words, for a conventional fluid to exhibit homogeneous isotropic turbulence, all velocity moments must be both translationally and rotationally invariant. One final statistical symmetry of particular interest in the study of turbulence is stationarity. A turbulent flow is said to be stationary if its mean values are independent of the time span over which the means are taken. High-Reynolds number turbulence in which these statistical symmetries are restored is known as fully developed turbulence.

Since plasmas are capable of sustaining electrical currents, energy can be dissipated either through viscosity or resistivity. Thus there are two sources of turbulence in plasmas. Resistive effects are characterized by another Reynolds number, given by

$$R_m = \frac{\mu_0 LV}{\eta}, \tag{2}$$

where η is a resistivity. Either effect can dominate the turbulent behavior of a plasma. Let R_e denote the original Reynolds number, characterizing viscous effects. Then the relative dominance of resistive dissipation in a plasma is given by the magnetic Prandtl number

$$P_{mag} = \frac{R_m}{R_e}. \tag{3}$$

As in conventional fluids, fully developed turbulence in plasmas is characterized by statistical homogeneity and isotropy. However, when dealing with plasmas the translationally and rotationally invariant moments of interest are usually those of the fluctuating magnetic field rather than a fluctuating velocity field.

Before discussing turbulence in magnetized plasmas in greater detail, it will be useful to discuss more historical background to the study of turbulence in fluid flows. Of particular relevance is the notion of a universal energy cascade and the use of frequency spectra to characterize turbulent systems.

2.1 Kolmogorov's 1941 Theory

In 1941, A. N. Kolmogorov published two papers which are widely regarded to have introduced the concepts of a universal energy cascade and of scale invariance to the study of turbulent flows, thereby founding modern turbulence theory [6]. The former concept is of primary importance here.

An energy cascade refers to a process in which energy introduced into a system at large scales nonlinearly couples to smaller scales, thereby distributing the system's energy over many length scales. This effect is often represented using energy frequency spectra. These time domain spectra can also be represented in a spatial domain using Taylor's hypothesis, which states that if velocity fluctuations in a system are small compared to the mean velocity, temporal variations in velocity can be reinterpreted as spatial variations of the velocity in the mean flow frame [7, 5]. In particular, energy cascades are often represented by their corresponding wavenumber spectra, here denoted $E(k)$.

One important result which follows from Kolmogorov's work on the universal character of energy cascades (although it is not explicitly derived in his papers) is that turbulent spectra obey a $-5/3$ power law scaling of over a large range of wavenumbers known as the inertial range. The following simple argument based on dimensional analysis demonstrates how this result is implied by the assumptions of Kolmogorov's 1941 theory in the case of turbulent velocity fluctuations.

Kolmogorov's theory was formulated on the assumption that the the energy wavenumber spectrum followed a power law depending only on k and an energy

transfer rate per unit mass, ϵ. In other words,

$$E(k) = Ck^{\alpha}\epsilon^{\beta} \tag{4}$$

for some constant α, β, and C. Note that if it takes energy some characteristic time τ to be transferred from one scale $1/k$ to the next, and v is the fluctuating component of the velocity, then $\epsilon \sim v^2/\tau$.

Given this power law assumption, we can apply dimensional analysis to arrive at the $-5/3$ character of $E(k)$. Now $\int E(k)\, dk = \langle v^2 \rangle$, so $E(k) \sim v^2/k$. Thus we have that

$$\frac{v^2}{k} \sim Ck^{\alpha}\epsilon^{\beta} \sim Ck^{\alpha}\left(\frac{v^2}{\tau}\right)^{\beta}. \tag{5}$$

Since τ has units of length over velocity, $\tau \sim 1/kv$, and thus we have

$$v^2 k^{-1} \sim k^{\alpha+\beta} v^{3\beta}. \tag{6}$$

Therefore $\beta = 2/3$ and $-1 = \alpha + \beta$, which implies that $\alpha = -5/3$. We can then express $E(k)$ as the $-5/3$ power spectrum

$$E(k) = Ck^{-5/3}\epsilon^{2/3}. \tag{7}$$

The inertial range in which this result holds corresponds to the range of scales at which energy dissipation effects due to viscosity are negligible, and extends from the energy injection scale to the so-called dissipation scale. One of the hypotheses of Kolmogorov's theory was that dissipation occurs on a length scale dependent only on the energy transfer rate ϵ and the viscosity ν [5]. It follows from this assumption that the demarcation between the end of the inertial range and the beginning of the dissipation range where viscous effects take hold is

$$L_k = \left(\frac{\nu^3}{\epsilon}\right)^{1/4}. \tag{8}$$

This is known as the Kolmogorov dissipation scale, or simply the Kolmogorov scale. A similar expression describes the end of the inertial range in the case of resistive dissipation, although the value depends on the particular dissipative mechanism assumed.

The argument for $-5/3$ power law scaling proceeds analogously for magnetic fluctuations, with $\epsilon \sim b^2/\tau$ (where b is the fluctuating component of the the magnetic field) and $E(k) \sim b^2/k$. However, it relies on the further assumption

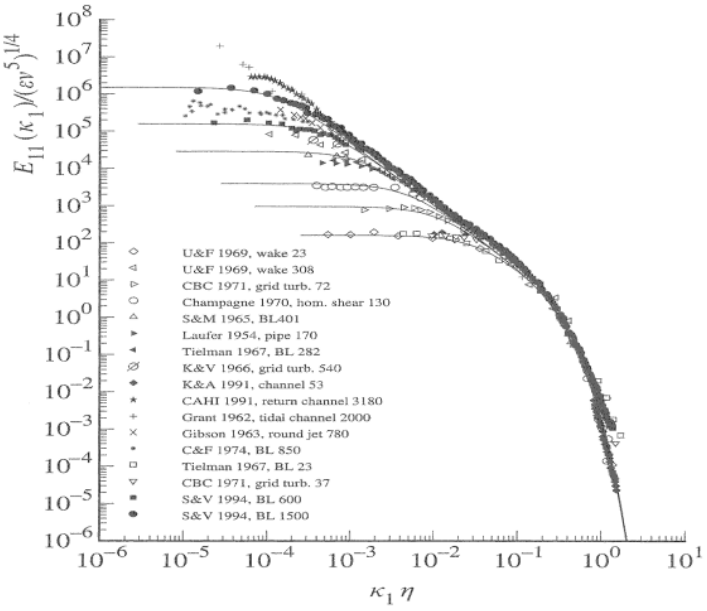

Figure 1: Normalized wavenumber spectra from a variety of conventional fluids, displaying the -5/3 Kolmogorov scaling. Source: [8].

that the time for energy to be transferred from one scale to another is determined by the Alfvén speed, v_A, which is proportional to b, implying that $\tau \sim 1/kb$. If modes faster than v_A are present, the energy transfer rate is increased, and we see deviations from the $-5/3$ scaling of the inertial range. Indeed, as will be seen in the next two sections, steeper power law scalings are observed in studies of both astrophysical and experimental plasma turbulence.

2.2 The Solar Wind

The solar wind is a continuous stream of charged particles (i.e. plasma) coming from the superhot upper atmosphere of the sun, known as the corona, and extending all the way to the outer edge of the solar system, called the heliosphere. While the existence of this plasma had been postulated much earlier [9], and even used to explain the behavior of comets [10], the solar wind could not be studied *in situ* until the 1960s, after the launch of the first satellites. Instruments on-board satellites have measured the density of the solar wind plasma to be very low, approximately 10 protons per cubic centimeter. With densities this low, the mean free path of charged particles in the solar wind is approximately 1 AU, the average

distance between the sun and earth. For satellites near 1 AU, this means that the plasma measured by their instruments is essentially collisionless. Satellite measurements have also found that the solar wind plasma can exhibit two distinct flow patterns, known as fast and slow solar wind. Fast stream wind is emitted from open coronal field lines, and has typical velocities of 450 km/s to 800 km/s. Slow wind originates from more complicated coronal structures, and normally flows at speeds less than 450 km/s [9]. In either case, the flow is supersonic- the Mach number in the solar wind is near 10.

Although there are variations between fast and slow streams, temperatures in the solar wind are on the order of 10^5 K, and magnetic fields are typically on the order of 10 nT. These fields result from currents flowing within the plasma, and are therefore convected along with the motion of the plasma. For this reason, solar wind plasma is said to be completely dynamical. As with most naturally occurring dynamical plasmas, the solar wind tends to obey an equipartition of thermal, magnetic, and flow energies. More formally, the plasma beta defined by

$$\beta = \frac{nkT}{B^2/2\mu_0} \tag{9}$$

is on the order of one at 1 AU, indicating that magnetic and thermal pressures in the solar wind are comparable at this distance.

One property of particular interest to turbulent studies of the solar wind is that the rate at which structures in the solar wind evolve is slow compared to the mean flow velocity. So for a satellite at a fixed position, in the time it takes for a particular pattern in the magnetic field or density distribution to sweep by the satellite, the change in these structures is generally negligible.This condition is known as Taylor's hypothesis, and is heavily relied on in traditional studies of solar wind turbulence.[1] In particular, Taylor's hypothesis allows for frequency information to be used to extract information about spatial structure. Consider a structure of size d passing a satellite probe at velocity V. If this structure remains essentially unchanged over the time d/V required for it to pass the probe, it will be registered as a frequency $f = V/d$, thereby encoding spatial information in a time domain. If we so desire, we could then safely translate this reading over into wavenumber, or k space, according to the relation $k = 2\pi f/V$.

[1] As mentioned earlier, for fluid fluid flows we can formally interpret Taylor's hypothesis as asserting that velocity fluctuations v in the mean velocity frame satisfy $v << V$, where V is the mean flow velocity. In the solar wind, V is typically hundreds of kilometers per second, while fluctuations in velocity, as well as density and magnetic field, are typically much slower, so the hypothesis generally pertains.

Turbulence in the Solar Wind

As the only astrophysical plasma which we can study *in situ*, the solar wind is a paradigm of plasma turbulence laboratories. The power laws obeyed by density, velocity, and magnetic field fluctuation spectra from the solar wind indicate that it exhibits nearly fully developed turbulence, despite being essentially collisionless. This is made possible by the waves propagating through solar wind plasma, which play an analogous role to the intermolecular collisions producing turbulence in conventional fluids. The resulting fluctuations are not only highly unpredictable, but highly stationary for hours or days at a time [11, 12]. The slow wind in particular is identified with well-developed turbulence, while the fast wind has fewer large scale structures and is often said to exhibit less evolved turbulence [13, 14]

Given the high velocities and astronomic scales characteristic of the solar wind, the magnetic Reynolds number R_m for plasma flows in the solar wind is on the order of 10^7. Reynolds numbers of this size are often either taken to be good indicators of well-developed turbulence, or simply to imply well-developed turbulence as a matter of definition. In either case, the identification is supported by other statistical indicators of turbulence.

Although the Reynolds number for the solar wind plasma is very large, and though it is bounded only by the magnetospheres of individual planets and the heliosphere surrounding the solar system, satellite measurements indicate that one statistical symmetry in the solar wind remains broken even as far from the sun as earth's orbit. Namely, magnetic fluctuations parallel to the mean field have lower variance than in any other direction [15]. Thus turbulent flows in the solar wind are anisotropic. This anisotropy is evident in many statistical studies of solar wind turbulence, such as frequency spectra, discussed next.

As an example of the spectral character of the solar wind, consider Figure 2 from Sahraoui, *et al* [16]. This frequency power spectrum was generated from three-hour, fast stream time series collected by the Cluster spacecraft. In order to cover a larger spectral range then previously studied, spectra from the Flux Gate Magnetometer (FGM) and STAFF Search-Coil (STAFF-SC) on-board the spacecraft were merged at $f = 1.5$ Hz. For both spectra, measurements perpendicular and parallel to the mean magnetic field are shown separately. As a result of the anisotropy of the solar wind, the perpendicular fluctuations are more energetic and thus shifted vertically from the parallel fluctuations. Since both directions display similar slopes, it would appear that this anisotropy does not depend on scale. Dotted black lines indicate noise levels, and solid black lines indicate power law fits.

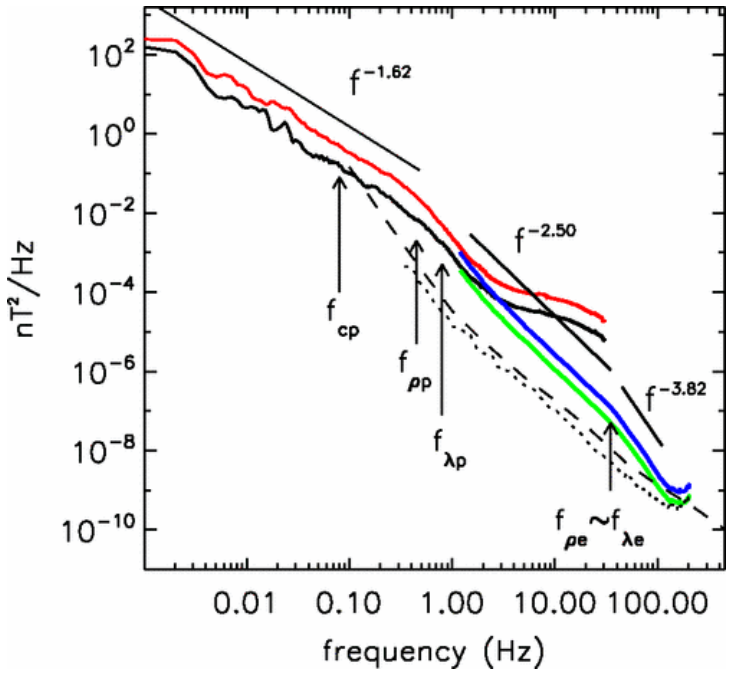

Figure 2: Typical frequency power spectra for magnetic fluctuations in the solar wind, generated from Cluster spacecraft data.

Much of the range covered by the FGM data displays a power law character consistent with the $-5/3$ prediction derived from Kolmogorov's 1941 hypotheses. However, a break point occurs near the (Doppler-shifted) proton gyrofrequency[2], marked f_{ρ_p}, and the magnetic energy spectrum continues with a new power law dependence down to the electron gyrofrequency f_{ρ_e}, after which it falls off sharply, likely due to dissipation effects. The source of these breakpoints and the power law character between f_{ρ_p} and f_{ρ_e} is discussed in [16], but for our present purposes it is sufficient to note the departure from neutral fluid turbulence, and the important role of frequency power spectra in the study of solar wind turbulence.

Further evidence of deviations from conventional fluid turbulence in the solar wind is provided by studies using the method of temporal increments. In a truly random signal, after some delay τ one would expect to see as many increases in the signal value as decreases, and large excursions should be rare. The deviation of magnetic time series from this expectation can be quantified by calculating

[2]The proton gyrofrequency, or cyclotron frequency, is the angular frequency of a proton's circular orbit about magnetic field lines in an approximately uniform field.

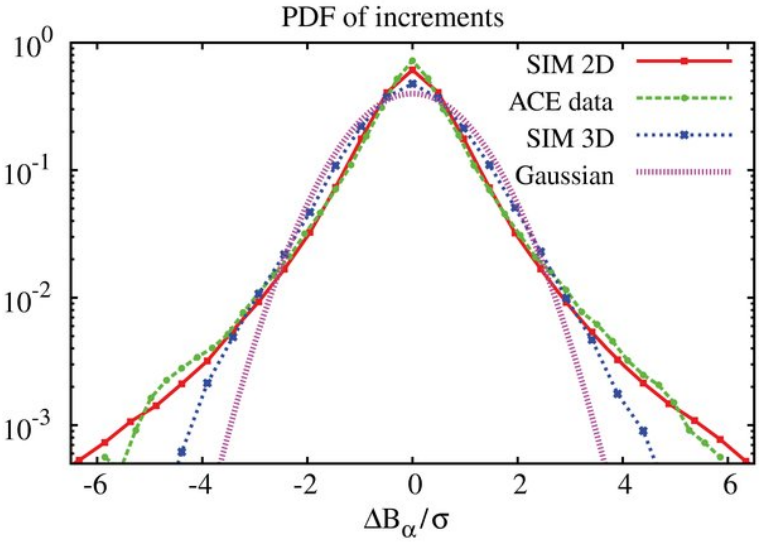

Figure 3: PDF of increments for one component of ACE spacecraft magnetic data and simulated data in 2-D and 3-D. A Gaussian distribution with the same mean and variance as the ACE data is shown for comparison.

increments

$$\Delta b = b(t+\tau) - b(t) \tag{10}$$

for values in the series and considering the probability mass function constructed from the record of these increments. This PDF should be closer to Gaussian the more random the corresponding time series. As fully developed turbulence in conventional fluids is highly stochastic, the presence of coherent structures in turbulent plasmas absent in turbulent neutral fluids can be detected by comparing the PDF of increments from a turbulent plasma source to fitted Gaussian distributions. For example, regions of high magnetic stress in plasma flows result in large, sharp changes in the increments of the signal, skewing the distribution towards the edges. It has been well-established that PDFs of increments for magnetic fluctuations in the solar wind are much wider than corresponding Gaussian distributions [17, 18, 19]. These "fat tails" are taken as good evidence for the presence of coherent structures in solar wind turbulence which are absent from conventional fluid turbulence. More quantitatively,

$$F(\tau) = < \Delta b^4 > / < \Delta b^2 >^2 \tag{11}$$

characterizes the flatness of a distribution, and while $F = 3$ for a Gaussian distribution, PDFs of increments from the solar wind can be as much as an order of magnitude flatter.

Figure 3 shows one such comparison between a PDF of increments from solar wind data and a Gaussian fit, from [20]. The increments distribution was constructed from one component of a 27-day magnetic signal from the ACE spacecraft, split into 12-hour subintervals. A delay of 4 minutes was used to compute each increment. In addition to the normalized PDF of increments for the ACE dataset and the Gaussian distribution, Figure 3 shows the PDFs of increments for data from both 2-D and 3-D simulations. The ACE data displays the "fat tails" expected, and most closely matches the 2-D simulation data. Analysis of this simulation indicated that many small-scale sheets of current between ropes of magnetic flux are the main source of this preponderance of large excursions from the mean.

Many of the statistical tools used to study solar wind turbulence yield similar results when applied to the MHD, or magnetohydrodynamic, turbulence in the plasma wind tunnel configuration of the Swarthmore Spheromak Experiment, which we turn to now.

2.3 The SSX MHD Plasma Wind Tunnel

Like the solar wind, the plasma studied in the MHD wind tunnel of the Swarthmore Spheromak Experiment (or SSX) is completely dynamical, as there is no applied magnetic field. Spheromaks, or donut shaped blobs of plasma, are generated by a discharge of pure hydrogen gas in a plasma gun. A high voltage is applied, ionizing the gas. The resulting current flow heats the plasma and accelerates the spheromak to speeds of about 50 km/s.

These plasma plumes have stored magnetic energies on the order of 1 kJ, and magnetic helicities which can be finely controlled by varying the magnetic flux through the core of the gun [21]. This gun flux is referred to as the "stuffing flux". Magnetic helicity corresponds to the degree of twistedness in the magnetic field, so varying injected helicity affects the resulting turbulent dynamics of the plasma as it evolves towards a relaxed helical state, known as a Taylor state [22, 23, 24]. This minimum energy Taylor state of the plasma is set by the boundary conditions in the device (i.e. a conducting cylinder). This relationship between injected helicity and the turbulence of the plasma's evolution into its minimum energy state will be explored further in Section 4.4. Note that the entire relaxation process takes only 10s of microseconds.

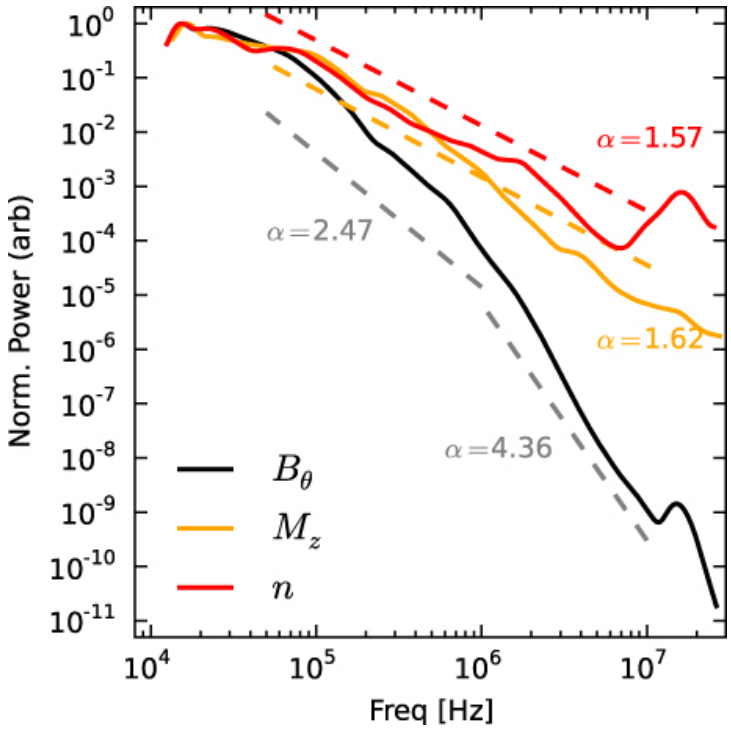

Figure 4: Power spectra for B-field, density, and Mach number fluctuations in the SSX MHD wind tunnel configuration, with fitted scaling exponents.

The body of the wind tunnel consists of a 1 m long cylindrical copper flux conserver with radius 0.08 m, equipped with probes to measure turbulent fluctuations in the evolving spheromak. Measurements of $\dot{B}$ acquired by a 16-channel, 3-direction, single-loop pickup coil probe array located at the midplane of the tunnel are used to study magnetic fluctuations. The probe array has a 65 MHz sampling rate and 14 bit dynamic range. The entire flux conserver is embedded in a high vacuum chamber. A cryogenic pump prepares the 10^{-8} torr vacuum.

Turbulence in the SSX MHD wind tunnel

Taking the tunnel radius as the characteristic length scale and typical mean velocities as characteristic, the magnetic Reynold's number R_m for plasma plumes in the SSX device is a few hundred. The exact value varies depending on which dissipation mechanisms are taken as primary, but the order of magnitude remains unchanged. Thus R_m for the SSX MHD wind tunnel is approximately five orders of magnitude less than R_m in the solar wind. In other words, the solar wind

exhibits more fully developed turbulence, with greater active degrees of freedom than SSX plasmas. Even so, the turbulent fluctuations in these two systems do display certain similarities when analyzed statistically.

As in the solar wind, turbulent fluctuations in the SSX MHD wind tunnel exhibit deviations from neutral fluid turbulence when studied in frequency or wavenumber space. Power spectra for SSX magnetic field, density, and Mach number fluctuations from [25] are shown in Figure 4. Note that magnetic field spectra are calculated by taking $\dot{B}$ spectra generated directly from exerimental time series and dividing by the square of the frequency. The shot-averaged spectra for the three magnetic field components indicate that magnetic fluctuations are isotropic, so only the θ component is shown. Only the Mach number spectrum, which serves as a proxy for the velocity spectrum, is very close to the $-5/3 \approx -1.66$ Kolmogorov scaling, with an exponent of -1.62. The other two quantities display steeper power law scalings, with the magnetic spectrum by far the steepest.The origin of this scaling and the break in the magnetic spectrum are not well-understood. However, the steeper scaling of this magnetic spectrum than the solar wind spectrum in Figure 3 may reflect a resistive dissipation mechanism that is present in SSX wind tunnel plasma but absent in the solar wind [25].

The method of temporal increments also shows similarities between turbulence in the solar wind and the SSX MHD wind tunnel. Figure 5(a) shows PDFs of increments for SSX $\dot{B}$ signals calculated for two different time steps τ, with fitted Gaussian curves for comparison. At the smaller time scale analyzed, the distributions are much broader and less Gaussian, indicating more large fluctuations at these scales. As the larger time scales considered, the PDFs are more Gaussian. These results suggest the presence of coherent structures, such as reconnection sites, at small scales, as is thought to be the case in the solar wind. This suggestion is further supported by simulations including such structures which display similar trends to the experimental data when analyzed using the increments approach [25].

Intermittency in SSX data also displays an interesting dependence on the helicity of the injected plasma plume. Figure 5(b) shows plots of the flatness of PDFs of temporal increments $F(\tau)$ over a wide range of time steps, at a variety of injected helicities. As observed earlier, when larger time steps are used, magnetic fluctuations begin to appear entirely uncorrelated. In other words, $F(\tau)$ approaches 3, the flatness of a random, Gaussian distribution. This trend appears across helicity settings, but there is also a general trend of increased flatness for greater helicities. The exact physical mechanism for this trend is unknown, but it appears that the value of the magnetic helicity of the injected plasma has impor-

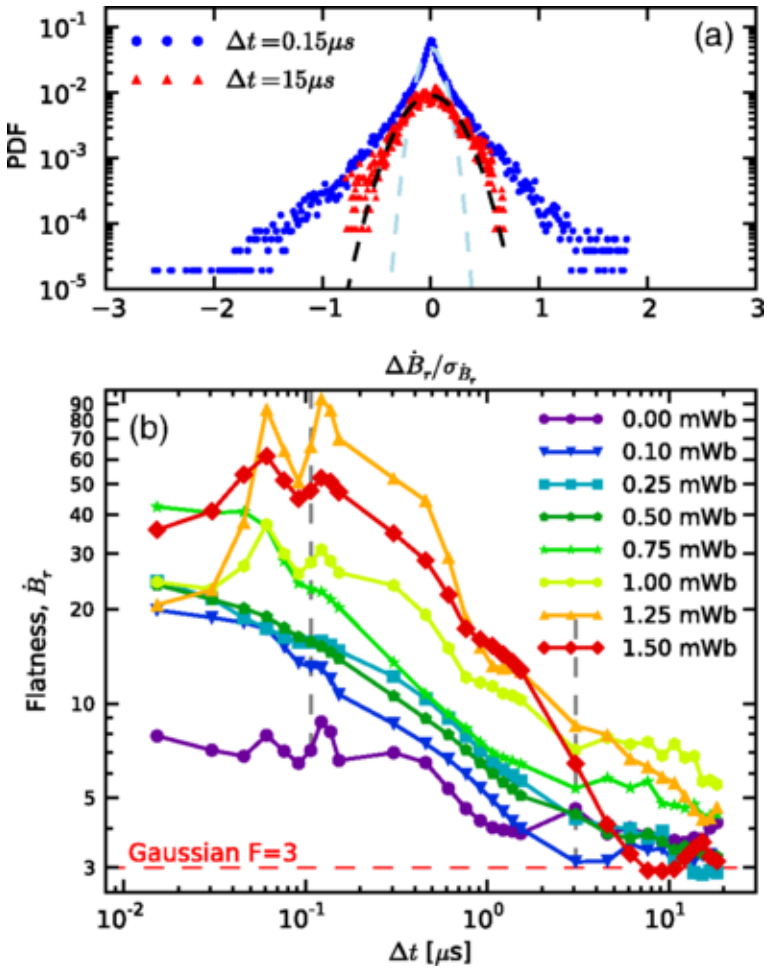

Figure 5: PDFs of temporal increments for magnetic fluctuations in the SSX MHD wind tunnel, using two different time steps. The fat tails of the distribution generated with a smaller step size indicate the presence of coherent structures at small time scales. When larger time scales are analyzed, the PDF becomes more Gaussian. Dashed lines indicate fitted Gaussian distributions. (b) Measures of flatness as a function of time scale, for a variety of helicity states. Only fluctuations in the radial magnetic field component were used here.

tant consequences for the frequency of large fluctuations in the resulting turbulent dynamics [23].

The dependence of the spectral character of SSX magnetic fluctuations on helicity are also studied in [23]. However, little or no difference in the frequency

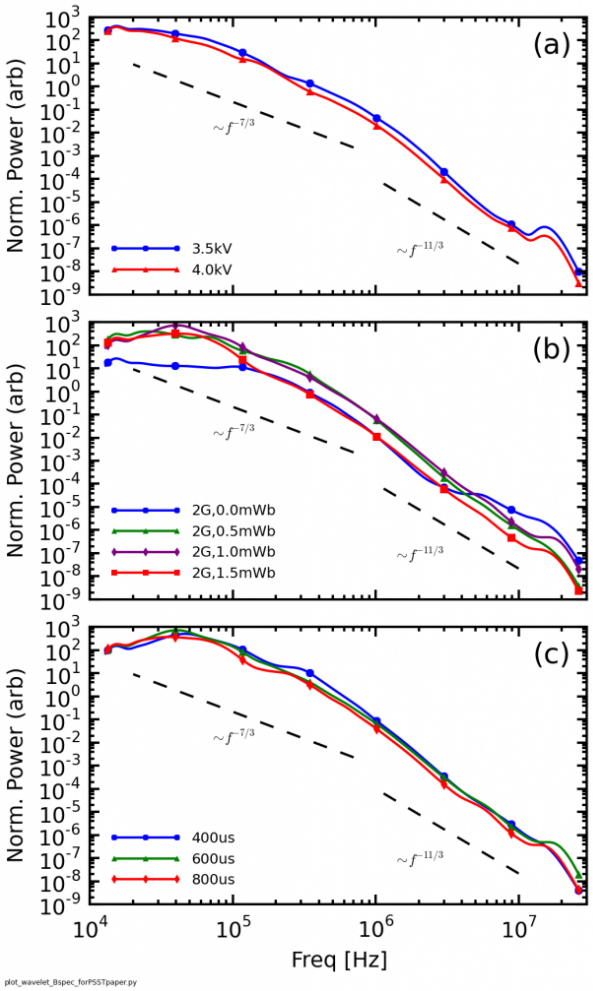

Figure 6: Comparison of spectra for three experimental parameters: (a) gun voltage, (b) stuffing flux, and (c) gas load.

power spectra for different helicity settings could be identified, suggesting that the same basic cascade process occurs irrelevant of the magnetic helicity.

SSX spectra also appear fairly robust to variations in other experimental parameters [26]. Figure 6 shows frequency spectra for several settings of the voltage applied to the plasma gun, the stuffing flux through the gun (closely connected to injected helicity, as mentioned earlier), and the gas shutoff delay, a proxy for the amount of hydrogen present in the gun during discharge. There is little variation in spectral character for changes in all of these parameters. Once again, this

suggests that the same basic turbulent cascade is occurs across settings. It would seem that either higher order moments, such as temporal increments, or more sophisticated statistical tools, such as measures of complexity, would be required to capture any dynamical changes taking place when such experimental parameters are varied. However, only the dependence of complexity measures on the stuffing flux parameter will be discussed here.

3 Measures of Entropy and Complexity

Physicists use many different metrics to quantify the uncertainty of probabilistic processes, although the Shannon entropy may be the most general. Given a discrete probability distribution $P = \{p_i : i = 1, \ldots, N\}$, Shannon's entropy is defined:

$$S[P] = -\sum_{i=1}^{N} p_i \log p_i \tag{12}$$

Where the product $0 \cdot \log(0)$ is taken to be 0, and the log is usually base 2 as a matter of convention. When normalized to its maximum value, the Shannon entropy is often denoted H. This definition is widely accepted as a measure of uncertainty, randomness, or information content in theoretical physics [27]. For example, while a prefect crystal can be described by a probability distribution centered around a single, dominant state, and is thus highly predictable, an ideal gas is equally likely to be found in any one of its accessible states, and is thus maximally unpredictable, or random. Put differently, while the amount of information needed to describe the perfect crystal (such as the distances between neighboring vertices and the symmetries of its structure) is quite small, the amount of information needed to specify the state of the ideal gas is maximal. These intuitive observations are quantified by the Shannon entropy, which would be minimal given the probability distribution associated with the perfect crystal and maximal for the uniform distribution associated with the accessible states of an ideal gas [28]. Note that for the ideal gas, the Shannon entropy actually yields Boltzmann's entropy as a special case: the Shannon entropy of the uniform distribution $P_e = \{\frac{1}{N}, \ldots, \frac{1}{N}\}$ is

$$S[P_e] = -\sum_{i=1}^{N} \frac{1}{N} \log \frac{1}{N} = -\log \frac{1}{N} = \log N, \tag{13}$$

where N denotes the number of accessible states. Since it was introduced as a general definition of entropy in the 1940s, Shannon's entropy has found a wide variety of applications across physics, mathematics, and information theory [29].

While efforts to formalize our intuitions about the order of a perfect crystal and randomness of an ideal gas in terms of entropy have largely been met with success, a general mathematical definition of the complexity of a physical system or process based on its probabilistic description have proven more elusive [27]. Unsurprisingly, the concept of complexity is rather complex, and may describe very

different statistical characteristics depending on the context in which it is applied. One particular kind of complexity, related to the notion of "non-triviality", is of interest here, as it constitutes the framework within which the Jensen-Shannon complexity will be defined.

Motivated by the intuitive identification of *both* the minimally entropic perfect crystal and maximally entropic ideal gas with minimal complexity, the authors of [28] proposed a general measure of complexity

$$C = HD, \tag{14}$$

where H is Shannon entropy and D is a quantity called a disequilibrium, quantifying how far a system's associated probability distribution is from the uniform distribution. For example, the perfect crystal would have a high disequilibrium, since only one state prevails, while the ideal gas would have minimal disequilib-

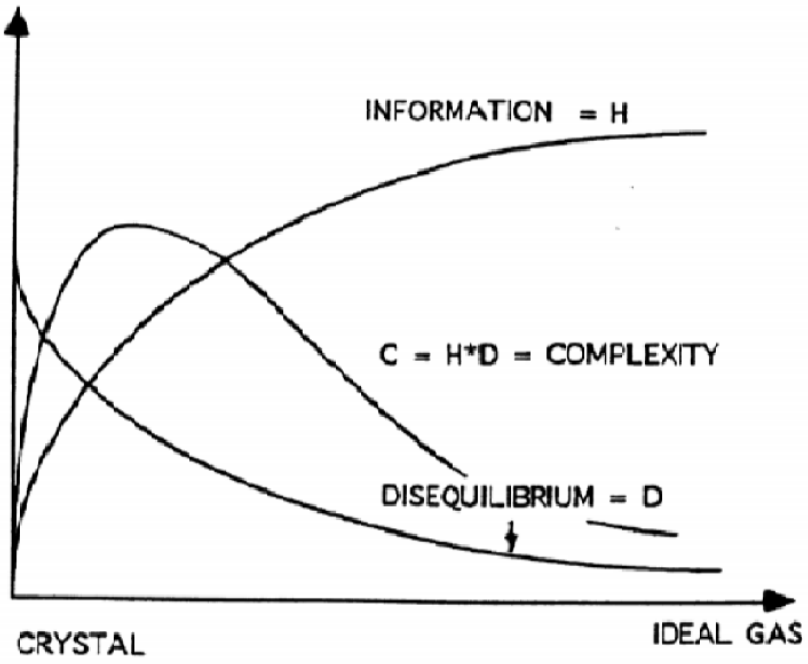

Figure 7: A graphical representation of the intuitive variations of "unpredictability" or "information content" (H) and "disequilibrium" (D) across different systems of particles. A general trajectory for $C = HD$, intended to capture the basic intuitive behavior of the notion of complexity, is also shown. Source: [28].

rium by construction. The logic to this definition of complexity can be illustrated graphically as in Figure 7. While both the crystal and ideal gas systems are low in complexity, one in virtue of its low entropy and the other its low disequilibrium, other, intermediate systems of particles can exhibit larger complexities.

This is all rather vague, but interpreting the more mathematically and operationally precise Jensen-Shannon complexity in later sections will be much more straightforward with this notion of complexity as a product of an entropy and a disequilibrium in mind. One last qualitative feature of statistical measures of complexity which I would like to highlight is that of scale. Defining complexity statistically in terms of a probability distribution across some accessible states introduces an inherent dependence on temporal or spatial scale, since more or less states may be accessible to a system depending on the scale at which it is considered. As we shall see, the dependence of statistical complexities of this form on scale is actually one of their great strengths, as this scale dependence may allow us to make inferences about particular physical mechanisms and the scales on which they operate.

3.1 the Permutation Entropy

The permutation entropy, PE, is just Shannon's entropy, S, from information theory applied to a specific probability distribution, which is sometimes called the ordinal pattern distribution. The ordinal pattern distribution is not defined for a given physical system *per se*, but a time series of equally spaced measurements of the system's state. We can think of the calculation of this distribution as a decomposition of the time series into its constituent ordinal patterns. Each probability in the distribution is the frequency of occurrence of one of the $n!$ possible ordinal patterns of n successive terms in the time series. Let's take a step back and introduce some formalism in order to clarify this definition.

Ordinal patterns

In the terminology used by Bandt and Pompe [30] and by Amigo [31], an ordinal pattern of length k is defined for a segment of a time series $\{x_0, \ldots, x_{k-1}\}$ as the permutation σ of the index set $\{0, 1, \ldots, k-1\}$ corresponding to the ranking of the x_i in ascending order, namely $x_{\sigma_0} < x_{\sigma_1} < \ldots < x_{\sigma_{k-1}}$.[3] For example, if our time series has three successive terms $x_0 = \sqrt{5}$, $x_1 = -3$, and $x_2 = \frac{1}{3}$, then since

[3] If $x_i = x_j$ where $i < j$, then in the ranking $x_i < x_j$ as a matter of convention.

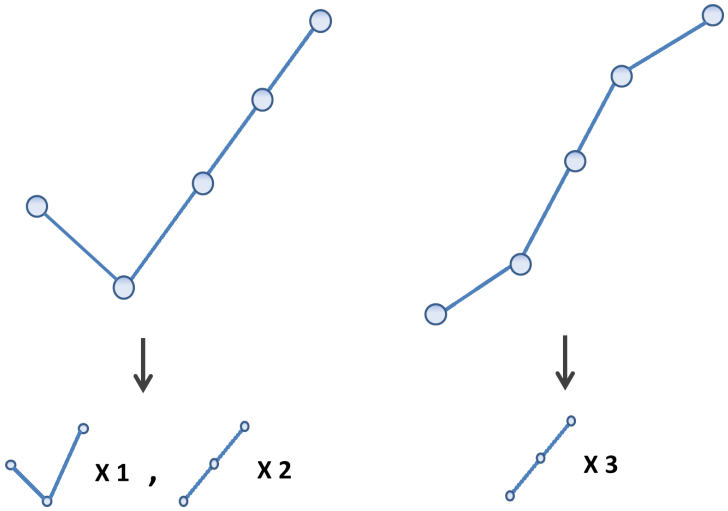

Figure 8: A graphical representation of two $L = 5$ time series, and their associated length $n = 3$ ordinal patterns. Note that the corresponding permutations would be 102 and 012.

$x_1 < x_2 < x_0$, our ordinal pattern is the permutation $\sigma = 120$. Another simple example is shown schematically in **??**.

The embedding dimension

Now, Bandt and Pompe's permutation entropy introduced in 2002 [30] is defined for a given order, or embedding dimension, called n. The order n permutation entropy for a given time series takes into account all and only ordinal patterns of length n appearing in the series. Thus we choose n based on what length patterns we care about. Given n, PE is calculated as Shannon's entropy for the probability distribution P_{ord} whose probabilities are given by

$$p(\sigma) = \frac{\text{number of length } n \text{ segments with ordinal pattern } \sigma}{\text{total number of length } n \text{ segments in the time series}}. \tag{15}$$

So each $p(\sigma)$ is calculated by considering all $L - n + 1$ segments n values long from a time series of length L and determining what fraction display the ordinal pattern σ. Since there are $n!$ permutations of n elements, there are $n!$ possible ordinal patterns σ and thus $n!$ probabilities in the ordinal pattern probability

distribution P_{ord}. Therefore the permutation entropy is given by

$$PE = S[P_{ord}] = -\sum^{n!} p(\sigma) \log p(\sigma) \tag{16}$$

Where the sum is over ordinal patterns σ and the log is base 2.

The embedding delay

Instead of considering consecutive points in calculating the ordinal pattern probability distribution for a time series, an embedding delay τ can be used to sample ordinal patterns on a larger time scale, thereby placing a lower limit on the temporal size of structures resolved, consequently limiting the maximum resolved frequency. Embedding delays can be implemented as a simple sub-sampling of data in which only L/τ values of the time series are considered [2, 3] or all portions of the original time series can be used [32], a method referred to here as the length-preserving method. For example, for an embedding delay $\tau = 10$ using the former approach, a new time series X' of length $L' = \frac{1}{10}L$ is generated by selecting every tenth value of the original series X and the ordinal pattern probability distribution calculated for that series in the usual manner. In the length-preserving method, segments $(x_t, x_{t+10}, \ldots, x_{t+10(n-1)})$ of X are used to calculate the ordinal pattern probability distribution, where t runs from 1 to $L - 10(n-1)$, thereby including the 9/10ths of the dataset thrown out in the first method. In general when using the length-preserving embedding delay, for a time series of length L

$$\#\text{ of length } n \text{ segments considered} = L - \tau(n-1). \tag{17}$$

Equivalently, this is the number of ordinal pattern counts which are used to construct the ordinal pattern probability distribution.

Which embedding delay method is used depends in part on the length of the time series in question. For practical reasons, the length-preserving method is used exclusively here. The choice of embedding delay will be discussed in more detail in Section 4.2.

Interpreting the permutation entropy

As Bandt and Pompe say of the permutation entropy, "this is the information contained in comparing n consecutive values of the time series" [30]. The more information contained in the ordinal structure of your typical length n segment of the series, the more uncertainty there is in the dynamics of the system. Note that

this uncertainty is small when the time series is skewed towards repeating just a few patterns in the relative values of consecutive terms and large when there is much diversity in the ordinal patterns of consecutive terms. In the extreme cases, $PE_{min} = 0$ for a monotonic time series with only one ordinal pattern, while $PE_{max} = \log(n!)$, for a purely random time series in which every possible length n ordinal pattern occurs with equal probability $p(\sigma) = 1/n!$.

In light of these extremes, the permutation entropy is often normalized as

$$PE_{norm} = PE/\log(n!) \tag{18}$$

so that $0 \leq PE_{norm} \leq 1$.

3.2 the Jensen-Shannon Complexity

While the permutation entropy quantifies the randomness in an arbitrary time series, a measure of statistical complexity such as the Jensen-Shannon complexity is required to quantify any additional physical structure which might be reflected in the probability distribution constructed from the signal. The Jensen-Shannon complexity, or C_{JS}, of the distribution P of N probabilities associated with a time series is defined as the product

$$C_{JS}[P] = Q_J[P, P_e]H[P], \tag{19}$$

Where $H[P]$ is the normalized Shannon entropy and the quantity $Q_J[P, P_e]$ is a measure of disequilibrium, where P_e is again the uniform distribution [33]. In other words, $Q_J[P, P_e]$ quantifies how different P is from an equiprobable distribution, characteristic of a system such as an isolated ideal gas [28]. Therefore the quantity $C_{JS}[P]$ will be nonzero only if there exist privileged states among those accessible to the system, and largest for a given entropy the further the distribution of accessible states is from uniform. Formally, once the disequilibrium is normalized such that $0 \leq C_{JS} \leq 1$, the Jensen-Shannon complexity can be expressed

$$C_{JS}[P] = -2\frac{S\left[\frac{P+P_e}{2}\right] - \frac{1}{2}S[P] - \frac{1}{2}S[P_e]}{\frac{N+1}{N}\log(N+1) - 2\log(2N) + \log(N)}H[P], \tag{20}$$

Where S denotes the unnormalized Shannon entropy. When using the Bandt-Pompe methodology, the distribution P associated with the time series is the distribution of length n ordinal patterns P_{ord}, so that

$$C_{JS} = C_{JS}[P_{ord}] = -2\frac{S[\frac{P_{ord}+P_e}{2}] - \frac{1}{2}PE - \frac{1}{2}\log(N)}{\frac{N+1}{N}\log(N+1) - 2\log(2N) + \log(N)}PE_{norm} \tag{21}$$

where $N = n!$. For brevity, the term "Jensen-Shannon complexity" or "complexity" will subsequently be used to refer to this quantity, although it would be more accurate to use "Jensen-Shannon permutation complexity".[4]

Interpreting the permutation complexity

When the ordinal pattern distribution is used, C_{JS} can be interpreted as a measure of the non-triviality of the frequencies of occurrence of ordinal patterns in the time series. This characteristic of the ordinal pattern distribution is not directly considered in the permutation entropy, so that "evaluating C_{JS} provides one important additional piece of information", quantifying "not only randomness but also the degree of correlational structures" [34].

In order to begin to develop some intuition about these metrics, it will useful to consider a few simple examples. The simplest would be a monotonic time series, say representing a line with positive slope. The only length n ordinal pattern appearing in this time series is the permutation (0,1,...,n), and thus the permutation entropy is $-1 \log 1 = 0$. The corresponding ordinal pattern probability distribution is far from a uniform distribution, with only one bin filled, so the disequilibrium is large. Nevertheless, C_{JS} is zero since PE is zero. The fact that a monotonic time series has zero complexity intuitively matches the characterization of the Jensen-Shannon Complexity as a measure of structure, or non-triviality. At the other extreme is a completely random time series, from a maximally stochastic system where every possible ordinal pattern occurs with equal frequency $1/n!$. By construction, such a series maximizes the permutation entropy, so that $PE = \log n!$. However, the disequilibrium is zero, so the C_{JS} also vanishes. This again intuitively fits with the identification of Jensen-Shannon complexity as a measure of correlational structure.

3.3 Rationale

When talking about mathematical measures of complexity and entropy, it is important to keep in mind that any particular definition we adopt represents an attempt to formalize our intuitions about randomness and complexity, and thus should not be expected to directly represent any physical characteristic of a given system such as magnetic field strength or velocity. That is not to say that im-

[4] Amigo and others have proposed the term "permutation complexity" in order to distinguish the general kind of complexity captured using ordinal analysis [31]. In this terminology, both PE and $C_{JS}[P_{ord}]$ measure aspects of the permutation complexity of the time series in question.

portant physical information could not be or is not contained in a mathematical randomness or complexity measure, just that these metrics represent the physics of a system rather indirectly.

With these words of caution behind us, the main reason for using the permutation entropy as a measure of randomness instead of other incarnations of Shannon's entropy or related metrics is that most classical measures ignore the temporal order of the terms in a time series, thereby leaving out potentially valuable causal information [29]. By constructing a probability distribution based on comparisons of successive terms in a series, the permutation approach incorporates temporal order and thus causal information. Furthermore, while classical measures often make assumptions about the system in question or are only suited to deal with particular kinds of systems [29], permutation entropy can be applied to arbitrary time series [30]. Practically speaking, permutation entropy also has the advantage of being computationally faster, simpler, and more robust to noise than most comparable metrics [34]. Since Bandt and Pompe's seminal paper was published in 2002, "the power and usefulness of this approach has been validated in many subsequent papers", applying the metric to a variety of theoretical, biological, economic, and physical systems [29]. For example, these metrics have been used to distinguish noise and determinism in mathematical models [35], track the effects of anesthesia and predict seizures based on the randomness of EEG signals [30, 36, 37, 38], inform economic policy [39, 40], identify distinct time scales in chaotic semiconductor lasers [41], and even to study the dynamics of El Niño [42]. In plasma physics, permutation entropy and complexity were used in [2] and [3] to study turbulence at the Large Plasma Device (commonly abbreviated as LAPD). These prior applications of the Jensen-Shannon complexity and permutation entropy to plasma physics suggested that they could potentially be used identify new or previously overlooked features of plasma experiments. The work presented here represents the first extension of these metrics to astrophysical plasma turbulence or MHD experiments like SSX. Furthermore, this research was the first comparing turbulence in different plasma sources using the permutation entropy and complexity.

As was touched on in the previous section, additional information can be gained when the permutation entropy is considered alongside the Jensen-Shannon complexity, calculated using the same ordinal pattern distribution of Bandt and Pompe. In particular, it has been shown that a plane with PE_{norm} on one axis and C_{JS} on the other accommodates well-known stochastic processes and chaotic systems in different planar regions [34]. This so-called CH plane [5] was used in

[5] C stands for Jensen-Shannon Complexity and H for normalized Shannon entropy, although

conjunction with more traditional methods (e.g. exponential power spectra) as a means of identifying chaotic vs. stochastic dynamics in plasma systems in the aforementioned work at LAPD [2, 3]. In addition to its demonstrated capability of distinguishing between noise and chaos, C_{JS} is preferable to many competing statistical complexities in virtue of the fact that it is an intensive quantity [33]. So if a system's dynamics have been captured by a time series of appropriate length and sampling rate, increasing the length of the series should not alter the value of C_{JS}.

3.4 Maximum and Minimum Complexity

As a non-trivial functional of the entropy, C_{JS} can take on a range of values for a given PE_{norm}. In particular, C_{JS} is constrained between well-defined bounds, which are shown for $n = 5$ by the crescent-shaped curves in Figures 9 and 10. These curves are derivable from equation (20) using undetermined Lagrange multipliers to maximize the complexity given fixed entropy as a constraint [43]. The results are summarized below.

For fixed entropy greater than 0 and less than 1, minimum complexity is attained when disequilibrium is minimal, i.e. when only one ordinal pattern is privileged and all $n! - 1$ others are equally likely. Four ordinal pattern probability distributions of this kind are shown in Figure 9, using $n = 5$ as a representative example. Note that instead of p_i, $-p_i \log p_i$ is shown on the vertical axis of the histograms, in order to improve readability. The associated positions for each of these distributions along the minimum complexity curve are shown in red in the CH plane on the right hand side of the figure. The possible values the privileged ordinal pattern frequency p can take on and the possible values of the remaining $n! - 1$ probabilities are of course constrained by the condition $\sum_{i=1}^{n!} p_i = 1$. The minimum complexity curve shown is generated by scanning over many possible values of p and calculating C_{JS} and PE_{norm} for each of the resulting ordinal pattern probability distributions.

As might be expected, the ordinal pattern distributions yielding the maximum complexity curve shown in black in Figure 10 are less straightforward. For fixed entropy, C_{JS} is maximized when the disequilibrium is maximized. However, in order to keep the entropy non-zero, more than one bin of the distribution must be filled. Among those probability bins which are non-empty, differing distributions of counts correspond to different entropies, so the particular value of the entropy

it should be noted that the ordinal pattern distribution in particular is used to calculate both quantities in these CH plane analyses

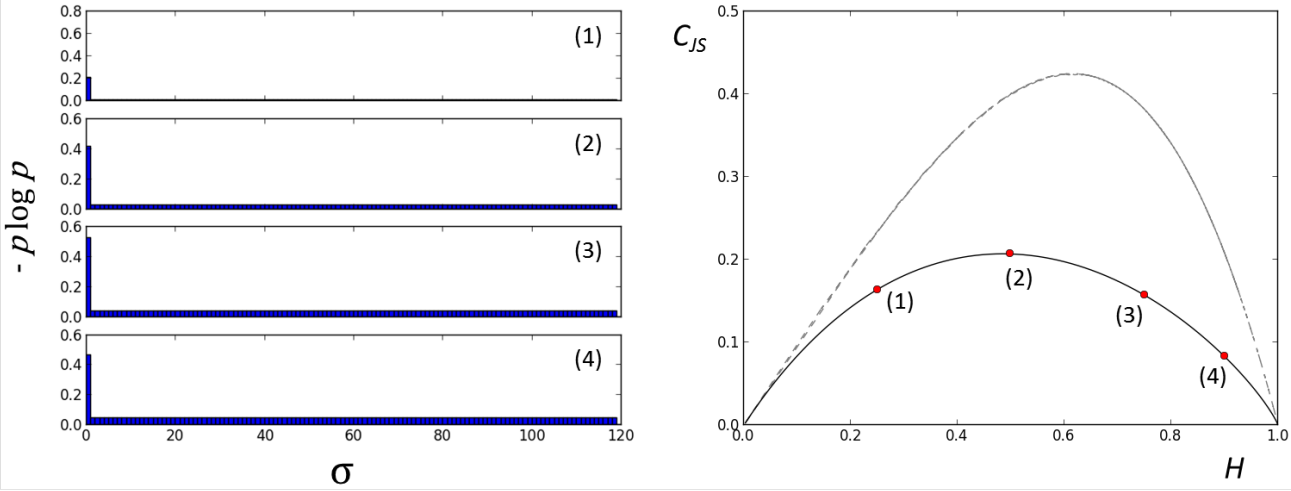

Figure 9: Minimum complexity bound on the CH plane is shown in black (right). Sample probability distributions from the family used to generate the curve are shown on the left, and their CH positions in red on the right.

puts some constraints on the number of bins and number of bins filled simultaneously. It turns out that the family of distributions which maximize the complexity over the full range of $PE_{norm} \in (0, 1)$ have some number N of patterns with for which $p_i = 0$, one pattern of unique probability p, and the remaining $n! - N - 1$ patterns with identical, nonzero probability, so that all probabilities sum to unity.[6] Technically, the maximum complexity bound is the envelope curve defined by the CH positions of all probability distributions from the family described. When 1,000 or more distributions from this infinite family are sampled and their CH positions plotted, a nearly smooth line across the top of the plane is formed without taking the envelope complexity, as shown in Figure 10. A few distributions from this family of maximally complex distributions and their associated positions on the CH plane are also shown, in red.

Based on the definition of complexity as a product of the entropy and a measure of disequilibrium, the crescent shape of these maximum and minimum complexity bounds makes good sense. We can make this connection more explicit by logi-

[6]In particular, the number of probabilities which are 0 must be $N = 0, 1, ..., n! - 2$, the value of the unique probability must satisfy $0 < p < 1/(n! - N)$, and all other probabilities p_j are given by $p_j = (1 - p)/(n! - N - 1)$.

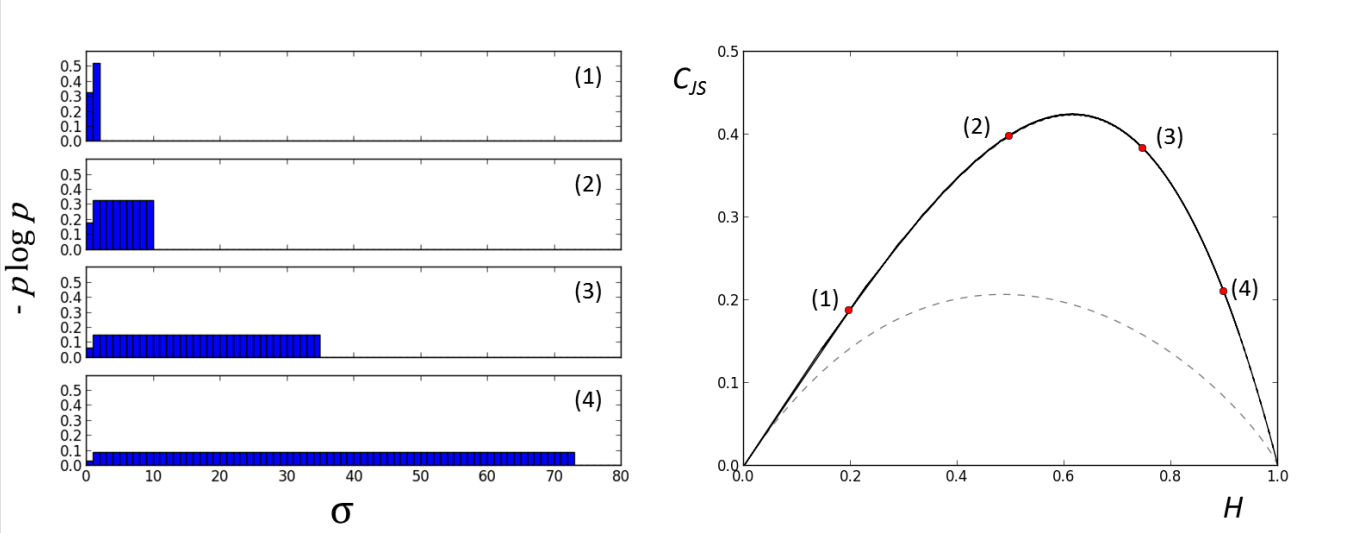

Figure 10: Maximum complexity bound on the CH plane is shown in black (right). Sample probability distributions from the family used to generate the curve are shown on the left, and their CH positions in red on the right.

cally tracing out the origin of the general arcing trajectory. By construction, the complexity is constrained to 0 at the $H = 0$ and $H = 1$ corners of the CH plane. Going from left to right, as we increase the entropy, the complexity exhibits a general increasing trend (due to the H term in the product HD), until we reach moderate entropies. At this point, we can think of the D term as "pulling down" the product HD- further increase in H requires the overall distribution of probabilities to fill out into all $n!$ accessible bins, resulting in low disequilibriums. These competing effects pinch the maximum and minimum curves together at the ends and result in a complexity maximum at intermediate entropies.

3.5 Reference Models and the CH Plane

The position of a fluctuating time series on the $PE_{\text{norm}} \times C_{JS}$ (or CH) plane simultaneously represents the unpredictability of the fluctuations and the degree of correlation between the frequencies of occurrence of these fluctuations in the series. Such a representation is desirable in large part because it is capable of differentiating between stochasticity and chaos, by accommodating these two types of dynamics in different regions of the CH plane. In order to interpret the implica-

tions of the CH positions of magnetic fluctuations in turbulent plasmas, it will be useful to develop some intuition about the plane. To this end, the CH positions of various mathematical models are examined. In particular, the CH positions of time series generated by (1) a simple sine function, (2) various chaotic systems of equations, and (3) a stochastic model known as fractional Brownian motion (or fBm) will be studied.

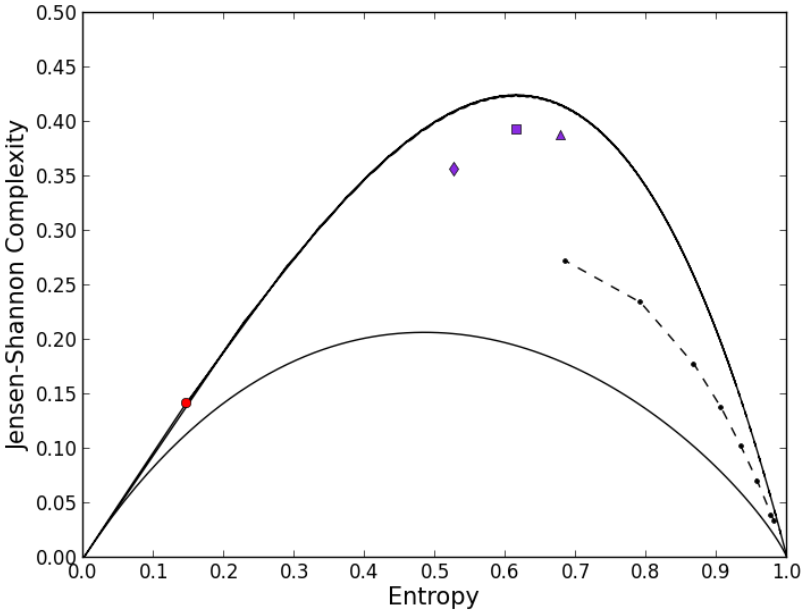

Figure 11: The $n = 5$ CH plane with various mathematical models, including a sine function (red circle), three chaotic maps (purple square, triangle, and diamond), and fractional Brownian motion for a range of Hurst exponents (dashed black line).

The sine function

The $n = 5$ CH position of a sine curve sampled in steps of $d = 0.001$ over one full period is marked in Figure 11 by a red circle. It is somewhat non-intuitive that a sine function would occupy this position of the plane, as it is right near the curve denoting maximum possible complexity, while sine is a very simple function. Indeed, if we were to base our measure of complexity on Fourier modes, a sine

wave would have minimum complexity. However, we are concerned here with ordinal patterns in consecutive, discrete values of a time series. If a sine curve is "discretized" by sampling some finite number of evenly spaced values over a range wider than π [7] to generate a time series the permutation entropy and complexity of this series will be necessarily non-zero.

For simplicity, consider the $n = 4$ case, with a time series generated by sampling a simple sine curve in steps of size d over one full period. When d is much less than π, the vast majority of length $n = 4$ ordinal patterns appearing in a sine time series will be either monotonically increasing (i.e. 0123) or monotonically decreasing (i.e. 3210), as the sine curve only deviates from this behavior at its maximum and minimum. However, the presence of maxima and minima necessarily introduce some additional ordinal patterns. When the full range spanned by a given ordinal pattern, τnd, is less than π, the distance from peak to trough, we can enumerate all possible non-monotonic ordinal patterns. Figure 12 shows four such ordinal patterns, corresponding to the peak in the curve. There are four more non-monotonic permutations corresponding to the trough of the sine curve. Thus in total there are 8 non-monotonic ordinal patterns which might appear in the time series, and a total of 10 accessible permutations for a sine curve sampled such that $\tau nd < \pi$. In the $n = 5$ case, there are 14 accessible permutations.

For example, consider a time series generated by discretizing the sine curve in steps of $d = 0.001$ from 0 to 2π. When analyzed with $n = 4$ and no embedding delay, only four out of the 6,280 ordinal patterns appearing in this time series were non-monotonic. The associated permutations were 3201, 0312, 2310, and 1203, the first two corresponding to the peak of the sine curve and the latter two the trough. The normalized permutation entropy and complexity of this time series was found to be $PE_{\text{norm}} = 0.22$ and $C_{JS} = 0.20$.

Note that were either d or τ increased for a series still spanning one full period, the overall number of ordinal patterns would decrease. However, so long as the condition $\tau nd < \pi$ is preserved, there would be no fewer non-monotonic ordinal patterns, as the presence of the peak and trough will always introduce at least four into the series. Thus the relative proportion of monotonic ordinal patterns would decrease, altering the permutation entropy and complexity. This point will be explored in more detail in Section 4.3.

On the other hand, in the limit as $d \to 0$ (and thus the length of the time series goes to infinity), the proportion of ordinal patterns which are monotonic approaches unity. Thus their contribution to the entropy approaches $-1 \log 1 =$

[7] π is significant as it is the distance from peak to trough, and thus the maximum range displaying only one ordinal behavior.

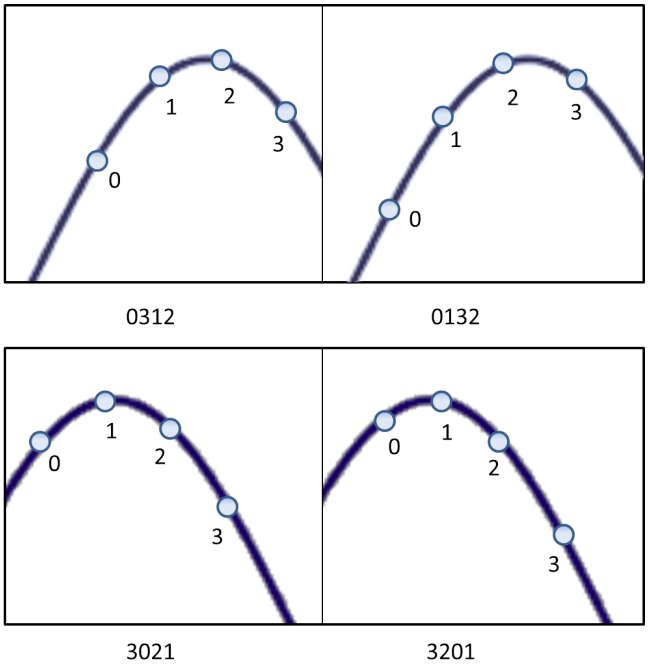

Figure 12: Examples of possible non-monotonic $n = 4$ ordinal patterns and their associated permutations for a sine curve with $\tau nd < \pi$.

0. Only a few non-monotonic patterns will appear irrespective of how small d becomes, so the proportion of non-monotonic ordinal patterns will approach 0, and since the limit as p approaches infinity of $p \log p$ is 0, these ordinal patterns will also make no contribution to the entropy. Therefore the permutation entropy and complexity of a sine function over a single period approach 0 in the limit of infinitesimally small sampling rates.

Chaotic Maps

Figure 11 includes the CH positions of three, paradigmatic chaotic maps. While deterministic chaos is highly unpredictable, reflected by moderately high entropies, there are intricate structures embedded in chaotic dynamics, reflected by near-maximal complexities on the CH-plane. A hallmark of mathematical chaos is the existence of *forbidden patterns* in the dynamics described by a system of equations [31]. As a result, fewer ordinal patterns are accessible to the system, and the disequilibrium is larger than it would be for most other processes with comparable uncertainty. For more information about chaos and the difference

between a chaotic and a stochastic system, see Appendix B.

These three chaotic maps are the Henon map, the skew tent map, and the logistic map. All three only exhibit chaos when the parameters in each model take on particular values, or values within a specific range. The definitions for each map, and the parameters used here, are as follows:

(1) The logistic map, which was originally developed in connection with population modeling, is given by

$$\Big\{ x_{n+1} = r x_n (1 - x_n) \tag{22}$$

$r = 4$ was used here, which puts the map in a chaotic regime. A time series is produced by setting some initial value x_1 and then iterating this equation with the parameter r held fixed.

(2) The Henon map, which can be viewed as a two-dimensional extension of the logistic map [34], is given by

$$\begin{cases} x_{n+1} = 1 - a x_n^2 + y_n \\ y_{n+1} = b x_n \end{cases} \tag{23}$$

where the model parameters a and b were set to 1.4 and 0.3 respectively, corresponding to a chaotic regime. If plotted in phase space (i.e. x-y space), this map with these parameters would generate a so-called strange attractor, with fractal dimensionality.

(3) The skew tent map, a continuous, piecewise function, is given by

$$\begin{cases} x/\omega & \text{for } x \in [0, \omega] \\ (1 - x)/(1 - \omega) & \text{for } x \in [\omega, 1] \end{cases} \tag{24}$$

$\omega = 0.1847$ is used here to generate chaotic time series sampled from this function.

These maps were iterated to generate time series of length $L = 10^5$ which were then used to calculate the complexities and entropies marked by the purple triangle, square and diamond in Figure 11. Note that x and y in the Henon map have the same fundamental ordinal structure, and consequently occupy the same position on the CH plane.

Fractional Brownian Motion

As a paradigmatic example of an inherently probabilistic, or stochastic, model, the CH positions of various fractional Brownian motion processes are shown in

Figure 11. fBm, is a generalization of Brownian motion, often represented $B^{\mathbb{H}}(t)$, where t is a real number greater than 0. While both processes are self-similar and Gaussian, Brownian motion has increments which are independent of one another, while in fBm increments $B^{\mathbb{H}}(t+1) - B^{\mathbb{H}}(t)$ need not be independent [34]. The correlation between increments is determined by a model parameter called the Hurst exponent, $\mathbb{H} \in (0,1)$. When $\mathbb{H} > 1/2$ increments are positively correlated, and when $\mathbb{H} < 1/2$ they are negatively correlated. $\mathbb{H} = 1/2$ corresponds to classical Brownian motion. The covariance for these stochastic models is given by

$$E\left(B^{\mathbb{H}}(t)B^{\mathbb{H}}(s)\right) = \frac{1}{2}\left(t^{2\mathbb{H}} + s^{2\mathbb{H}} - |t-s|^{2\mathbb{H}}\right), \tag{25}$$

where $s, t \in \mathbb{R}$, and $E(...)$ denotes the expectation value.

Fractional Brownian motion time series were generated for eight different Hurst exponents over a representative range, $\mathbb{H} = 0.1$ to $\mathbb{H} = 0.8$ in steps of 0.1. Each time series was 10^3 values long. The CH positions of these time series are connected by a dashed black line in Figure 11. As we might expect, longer memory fBm (i.e. positive correlation between increments) displays greater complexities, tending towards the middle of the plane. When increments are independent as in ordinary Brownian motion, the model is high entropy and relatively low complexity ($H \sim 0.9$, $C \sim 0.18$). Negative increments push the model closer to the stochastic limit, $H = 1$, $C = 0$. Interestingly, as found in Rosso *et al*, Gaussian processes such as fBm models tend to exhibit slightly lower complexity than comparable non-Gaussian processes. These models were selected here as representative stochastic processes in large part due to their Gaussian character, and fairly wide range of ordinal behavior.

4 Permutation Analysis of Turbulence Data

4.1 Datasets

Data from four different sources of turbulent plasma were studied using the CH plane methodology: solar wind data collected by the WIND spacecraft, SSX MHD wind tunnel data, a dataset from the Large Plasma Device (LAPD) at the University of California, Los Angeles, and a single time series from a liquid metal experiment at the University of Wisconsin-Madison. In this section, basic descriptions are given for each of these datasets.

WIND data

The WIND spacecraft is a satellite positioned near 1 AU, equipped to measure fluctuations in all three orthogonal components of the magnetic field as streams of solar wind plasma blow by. Measurements are made using a flux gate magnetometer, which provides a DC magnetic field measurement by recording the bias required for zero current to flow in a coil of wire subjected to a changing magnetic field. The sampling rate of the resulting time series is 3 s.

Multi-day long time series from a fast wind stream (Jan 14 - Jan 21 2008) and a slow wind stream (Jan 24 - Jan 29 2010) with large scale magnetic fluctuations on the order of 10 nT are analyzed here. The fast stream magnetic signal consisted of almost $230,000$ values, and the slow stream signal of over $170,000$. Both signals were highly stationary. As discussed in Section 2, this means that mean values were independent of the time span over which the mean was taken, and thus that a set of subseries could be treated as an ensemble. It will be noted whenever the time series are partitioned in this way.

SSX data

Magnetic fluctuations in the SSX MHD wind tunnel are measured by 16-channel, 3-direction, single-loop pickup coils. These coils actually measure $\dot{B}$ fluctuations, sampled at a rate of 65 MHz. The $\dot{B}$ time series can be used to generate B data, but the integration process artificially smooths the fluctuations. For this reason, the CH analyses presented here focus on $\dot{B}$ time series, although B series are also briefly considered. The dataset studied here consisted of $\dot{B}$ fluctuations acquired at 8 different stuffing flux settings. About 40 runs were done at each setting. Since the pickup coil probe array has 16 channels, corresponding to 16 different radial positions in the midplane of the tunnel, and each channel measures fluctuations

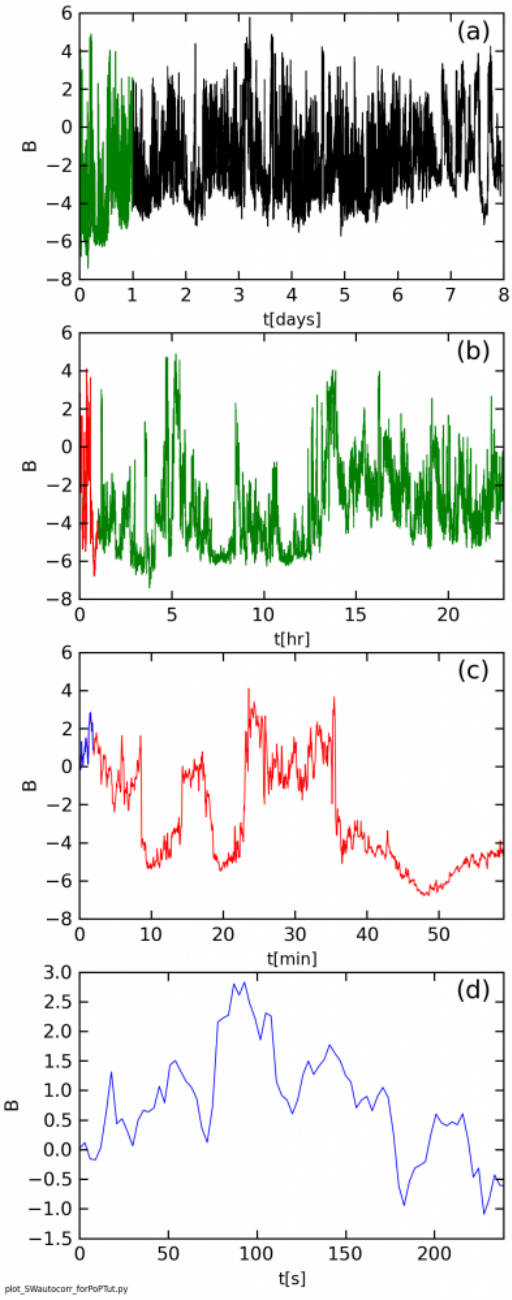

Figure 13: The fast wind B_x (in the radial direction outward from the sun) time series on the scale of (a) days, (b) hours, (c) minutes and (d) seconds. Each successive subplot shows a close-up of the section of the prior subplot plotted in a matching color.

in all 3 components of the magnetic field, the dataset consisted of a total of about $8 \times 40 \times 16 \times 3 = 15360$ $\dot{B}$ time series.

A single "shot" by the plasma gun lasts approximately $100\mu s$. The first $40\mu s$ or so are the "build up" phase, before the plasma has reached the tunnel midplane. After the plasma reaches the midplane, there is a relaxation phase, lasting about $20\mu s$. This 40 to $60\mu s$ window after the initial discharge is primary source of statistics for SSX turbulence studies. $\dot{B}$ time series spanning this window are 1300 values long, and fairly stationary. Unless otherwise noted, these are the series used to study the position of SSX magnetic fluctuations on the CH plane.

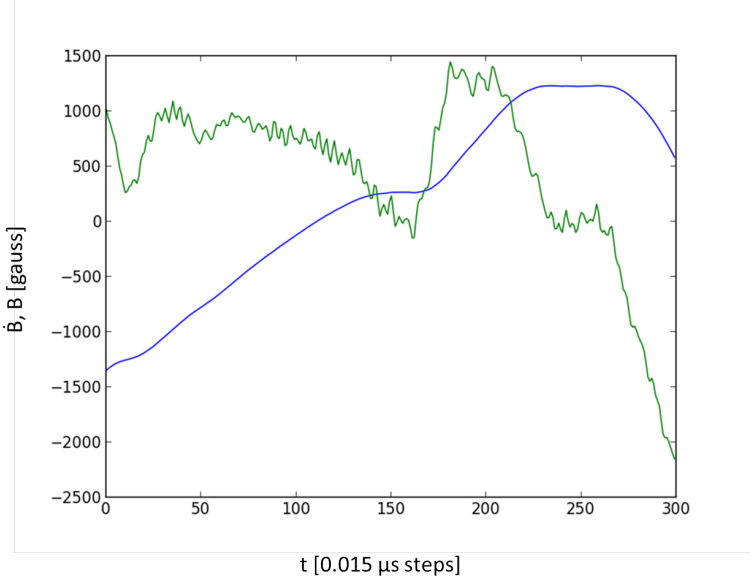

Figure 14: 4.5 microsecond portion of an SSX $\dot{B}$ time series (green) and the corresponding integrated B time series (blue).

LAPD data

The LAPD device consists of a 20-meter long, 1 meter diameter cylindrical vacuum chamber, in which plasmas are produced from a cathode-anode discharge from one end. A series of large electromagnets encircling the chamber provide a background field which can be varied in strength from 400 gauss to 2.5 kilogauss. Densities in LAPD plasmas are on the order of $10^{12} cm^{-3}$, and temperatures generally a few eV.

The LAPD time series studied here are ion saturation current signals acquired by probes inserted radially into the device.[44] Measurements of ion saturation current (or $I_{\rm sat}$) fluctuations within a probe provide information about several important plasma parameters, including magnetic field and temperature, although here $I_{\rm sat}$ time series are treated as surrogates for magnetic signals. Each such time series was sampled at 1.5 MHz, from a radial location of $26cm$ [45]. This corresponds to the outer edge of the plasma, where fluctuations are dominated by nonlinear interactions between waves generated by the pressure gradients that naturally develop between the plasma near the center of the device and the plasma near the chamber wall [46].

Time series from 25 shots on the LAPD device are used, each 5000 values in length. Previous work using frequency spectra has suggested that the edge fluctuations of magnetized plasmas in the LAPD and other similar devices are chaotic in nature [47], so the expectation was that LAPD time series would occupy a region of the CH plane closer to chaotic maps than the other plasma datasets analyzed.

Liquid Metal data

The fourth dataset studied was from a liquid metal experiment at the University of Wisconsin-Madison, constructed to study the dynamo effect. The experiment consisted of a 1 m diameter spherical vessel filled with liquid sodium, which was stirred to generate a turbulent flow whose inductive response could be probed with an applied magnetic field [48]. Due to the low kinematic viscosities ν in the experiment, the magnetic Prandtl number

$$P_{mag} = \frac{R_m}{R_e} = \frac{\nu}{\eta} \tag{26}$$

was small (about 9×10^{-4}). However, the magnetic Reynolds number R_m was on the order of 100 [48]. Such a small P_{mag} and relatively large R_m corresponds to an extremely large $R_e = LV/\nu$ Reynolds number, on the order of 10^5. The liquid metal experiment is therefore highly turbulent, with high flow speeds dominating viscous effects and magnifying small scale perturbations into unpredictable large scale fluctuations. It was anticipated that this unpredictability in the liquid sodium flows would carry over into unpredictable fluctuations of the magnetic field, reflected by a CH position comparable to stochastic systems. Magnetic time series from this experiment were generated by magnetic Hall-effect probes, at a sampling rate of 1 kHz. Signals were sent through a low-pass filter to reduce the

noise level before being digitized. Only one such time series, 16,380 values in length, was analyzed here.

4.2 Parameter Selection

The values of PE and C_{JS} for a given time series are strongly dependent on the parameters used to calculate these quantities. The primary parameters determining these values, and thus the CH position of the system, are the embedding dimension n and the embedding delay τ. In certain situations, it is also useful to consider the length L of the time series as a parameter jointly determining the CH position with n and τ. The obvious question then arises: how should these parameters be chosen? The answer depends on the nature of the research question being explored. For example, if the CH methodology is being used to identify particular time scales associated with different physical mechanisms, then n and L are often held fixed and the embedding delay varied, as in [49] or [50]. We are also interested here in more general questions of the relative randomness and complexity of time series from different physical systems. For these applications, the selection of τ and n is determined (or at least constrained) by a combination of practical limitations and physical, application specific considerations. Unfortuately, the use of the CH plane in plasma physics is not yet well-established, so there is no agreed upon formula for parameter selection specific to characterization and comparison of turbulent plasmas.

Practical considerations

In their seminal paper, [30], Bandt and Pompe recommend embedding dimensions n between 3 and 7, for "practical purposes". Even $n = 3$ captures very little of a time series ordinal dynamics, only considering $3! = 6$ permutations. In general, larger values of n seem preferable, in order to capture what longer correlational structures might appear. However, the length of a time series and the computational speed required for the application strongly limit the use of large n, hence Bandt and Pompe's recommendation of embedding dimensions less than or equal to 7.

Length is an especially important consideration here, since the SSX time series used are only 1300 values long. Unless $L \gg n$, the number of length n segments $L-\tau(n-1)$ in the time series will not be sufficient to "fill out" the ordinal pattern probability distribution in accordance with the true dynamics of the system. This will tend to artificially decrease the entropy of the signal. For this reason, it is often recommended that n be selected such that $L > 5n!$ [51]. In any CH

analysis presented here involving SSX data, $n = 5$ is used, in accordance with this condition. The time series from the other three systems are sufficiently long to warrant the use of an $n = 6$ embedding dimension, and the solar wind series so long that $n = 7$ is reasonable, but the focus here will be on the $n = 5$ CH plane so that comparisons can be drawn with magnetic fluctuations in SSX. $n = 5$ is preferable to smaller embedding dimensions since as noted earlier, smaller dimensions reflect only a few, relatively simple possible ordinal dynamics, and appear less capable of differentiating between systems.

Practical considerations similarly limit the size of the embedding delay τ. The number of ordinal pattern counts $L - \tau(n-1)$ going into the calculation of the distribution will also become too small if large embedding delays are used, artificially shifting the CH position of the time series. This phenomenon is explored in greater detail in the next section, but for now it suffices to note that for a given system there is a maximum delay beyond which the effect of insufficient statistics on the values of PE and C_{JS} becomes especially pronounced.

Physical considerations

System-specific physical considerations can also guide the choice of parameters. For example, perhaps there is a minimum n which is needed to appropriately distinguish the system from other systems. More commonly, it is the choice of the embedding delay which is guided by the system in question. If a particular physical mechanism or mode is of interest, τ should be selected so that the effective sampling rate is comparable to the frequency of the phenomenon in question. Going in the other direction, scales of interest can be identified based on local extrema in the entropy and complexity at particular values of τ [49]. In general, τ should be selected such that time scales of interest are larger than τ/f_{sample}, or equivalently, so that the range of frequencies of interest lies both below and near to f_{sample}/τ. The system specific considerations for the datasets analyzed here will be described in detail later. For now it suffices to note that the cadence of the WIND dataset forces us to consider frequencies in or below the inertial range in choosing τ, while SSX data is limited to a dissipation range and further constrained by the existence of a high-frequency noise mode. In the LAPD dataset, the optimal choice of τ will be determined by the existence of important modes in the plasma at relatively small time scales.

4.3 Effect of the Embedding Delay on CH position

Delay studies of a simple sine function

In order to better understand the role of the embedding delay in determining the CH position of a given system, time series generated by a simple sine function were analyzed. For all studies presented in this section, time series were generated by evaluating the sine function from Python's math module over a discrete range of evenly spaced values. Both the number of points used (i.e. the length of the time series) and the step size were varied, but the underlying system was the same period 2π sine function in all cases. In a sense, these sine time series can be regarded as a highly simplified model for time series collected at varied sampling rates and time spans from a physical system with some inherent time scale. Thus understanding the effect of the embedding delay on the entropy and complexity of these model time series could be informative about general relationships between the delay, the inherent time scale of the system in question, and the sampling rate and length of time series collected from the system.

First, a few general words about systems with inherent time scales are in order. When the range τnd of a given ordinal pattern becomes larger than the inherent time scale of a system, the permutation entropy and complexity will no longer be "seeing" the inherent ordinal behavior. This effect can be thought of analogously to aliasing. Exactly how it should be manifested in the CH position of the time series may not be clear a priori, so it will be treated in some detail. On the other hand, in systems with high frequency noise contamination, the essential dynamics will also be obscured if τnd is too small compared to the inherent time scale. This effect will be demonstrated by adding noise to a simple sine time series and considering the effect of the embedding delay on shifting the position of the series into the appropriate periodic region of the plane.

The analogue of an inherent time scale for the sine function might be considered to be 2π, the period of the function, or more appropriately for our purposes, π, since as noted in Section 4.3, this is the maximum ordinal range over which the simple monotonic permutations characteristic of the sine curve are accurately captured. Thus for scans of the embedding delay with fixed n and step size d, we expect the embedding delay τ_c satisfying $\tau_c nd = \pi$, or

$$\tau_c = \frac{\pi}{nd}, \tag{27}$$

to be significant. In particular, delays larger than τ_c will yield artificially diverse distributions of ordinal patterns, while for time series with added noise, delays

much less than τ_c will appear overly stochastic, with much broader distributions of ordinal patterns.

The first study conducted with these simple sine time series was to vary the quantity of data while holding the range of behavior analyzed constant. For example, one time series was generated by sampling the sine function between 0 and 10 in multiples of 10^{-4} (resulting in a time series of length $L = 10^5$), and another by sampling over the same 0 to 10 domain but in steps of 10^{-3} (resulting in a time series $L = 10^4$ values long). Since both 10^{-4} and 10^{-3} are orders of magnitude smaller than π, the expectation was that both these time series would provide reasonably good statistics over a large range of embedding delays (τ_c defined above is on the order of 6000 for the $d = 10^{-4}$ case and ≈ 628 for the $d = 10^{-3}$ series).

A scan with the $d = 10^{-4}$ time series of delays ranging from $\tau = 1$ to $\tau = 1000$ in steps of 50 is shown in Figure 15(a), and a scan over the same range of delays with the $d = 10^{-3}$ series is shown in 15(b) The CH position of longer time series with smaller step size does not display significant dependence on embedding delay, although there is a clear trend to increased complexity and entropy as τ is increased. This makes sense when the permutations in a sine curve are thought about qualitatively. The finer the sine function is sampled, the greater proportion of all permutations will be the monotonic 01234 and 43210 permutations. This is because a sine curve over a finite domain only departs from continuously increasing or decreasing behavior at the maxima and minima, as discussed in Section 4.3. Conversely, as the embedding delay is increased, the proportion of ordinal patterns representing the basic monotonic permutations will go down. This effect is exaggerated for the $d = 10^{-3}$ series shown in 8(b) by the larger step size used to generate the time series, as can be seen looking at the resulting ordinal pattern probability distribution. Figure 16(a) shows the ordinal pattern probability distribution of the $d = 10^{-3}$ series for $\tau = 100 < \tau_c$, 16(b) the distribution for $\tau = 628 \approx \tau_c$, and 16(c) for $\tau = 800 > \tau_c$. For $\tau < \tau_c$, the vast majority of patterns are monotonic, as expected. However, for delays near τ_c, the frequencies of monotonic and non-monotonic ordinal patterns become comparable, and thus the distribution more uniform. For $\tau = 800$, the distribution is even more uniform, while still limited to the 14 permutations accessible to a sine time series. Increased uniformity causes PE to increase. However, since the accessible permutations are still only a fraction of the 120 permutations of order $n = 5$, the ordinal pattern probability distribution remains far from a true uniform distribution. Thus the disequilibrium of the distribution remains more or less unchanged,

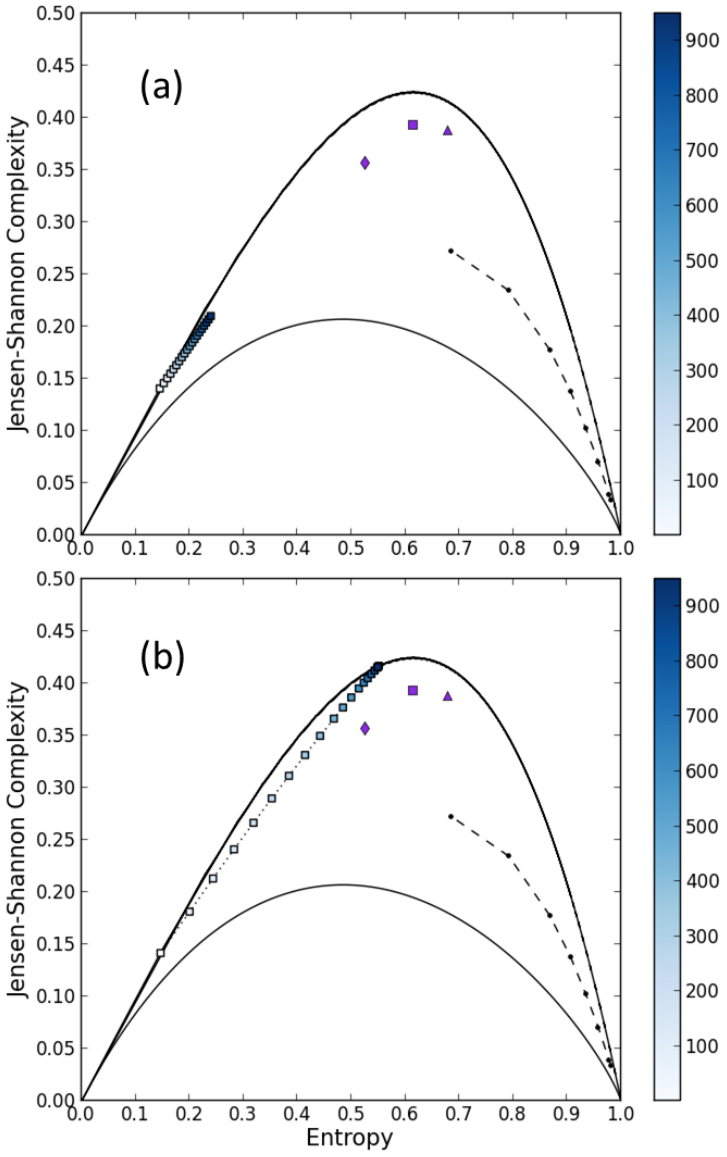

Figure 15: (a) $n = 5$ CH positions of a time series generated from a sine functions in steps of $d = 10^{-4}$ for a range of embedding delays. (b) CH positions of a sine time series generated with $d = 10^{-3}$ over the same range of embedding delays. Chaotic maps are shown in purple and fBm in dotted black for reference.

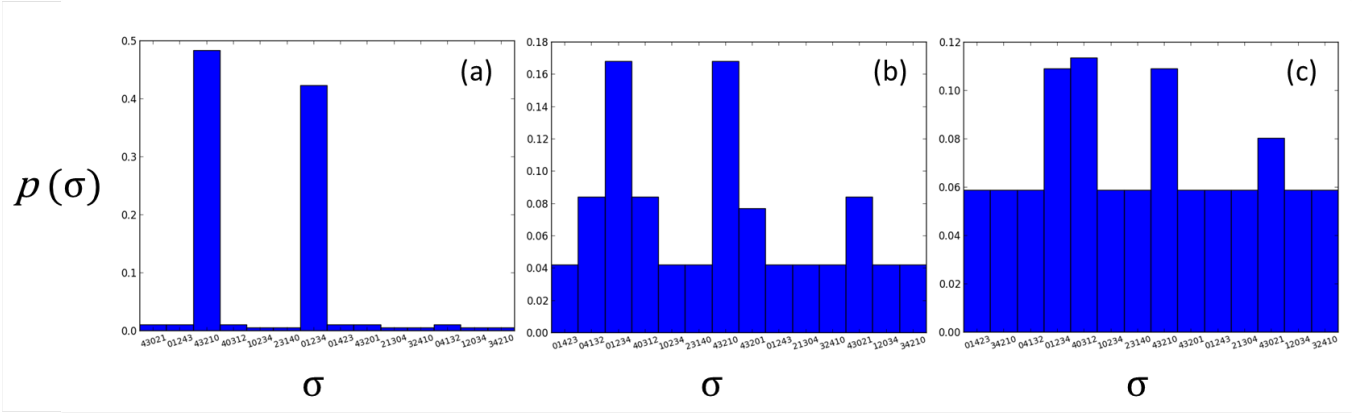

Figure 16: Ordinal pattern probability distributions of the $d = 10^{-3}$ sine time series for $n = 5$ and (a) $\tau = 100$, (b) $\tau = 628$, and (c) $\tau = 800$.

and the complexity increases roughly in proportion to the entropy, in accordance with equation (14), or equivalently (19). The almost linear relationship between complexity and entropy in Figure 15 is therefore to be expected.

Note that for delays near τ_c, this effect is sufficient to inflate the complexity and entropy of the $d = 10^{-3}$, $L = 10^4$ sine time series near to that of the chaotic maps. This does not reflect the underlying dynamics of the sine function (of course) or a failure of the CH methodology, but our choice of step size and embedding delay.

Interestingly, if the embedding delay is scanned over an even larger range, the CH trajectory of the series undergoes a leftward "hook" and starts to decrease in both entropy and complexity. This phenomenon is shown in Figure 17, for a scan of the embedding delay up to $\tau = 2500$ in steps of 100 with the $d = 10^{-3}$ series. An almost identical plot is generated if the time series spans the same range but with an order of magnitude larger or smaller step size and corresponding order of magnitude larger or smaller delays. For the $d = 10^{-3}$ series, the hook occurs near $\tau = 1000$. The ordinal pattern probability histograms indicate that for delays much larger than this, the total number of different permutations appearing in the signal is actually less than 14. Because at these delays the ordinal range is on the order of two periods, the permutations which do appear are often different from the 14 permutations accessible to a series satisfying $\tau n d < \pi$. However, limitations in the range of the full series constrain them to just a few newly accessible permutations. As the delays are increased further, these constraints become more stringent, and fewer and fewer different permutations appear. This reduces the entropy, resulting in the reversed trend after the hook. Eventually, the

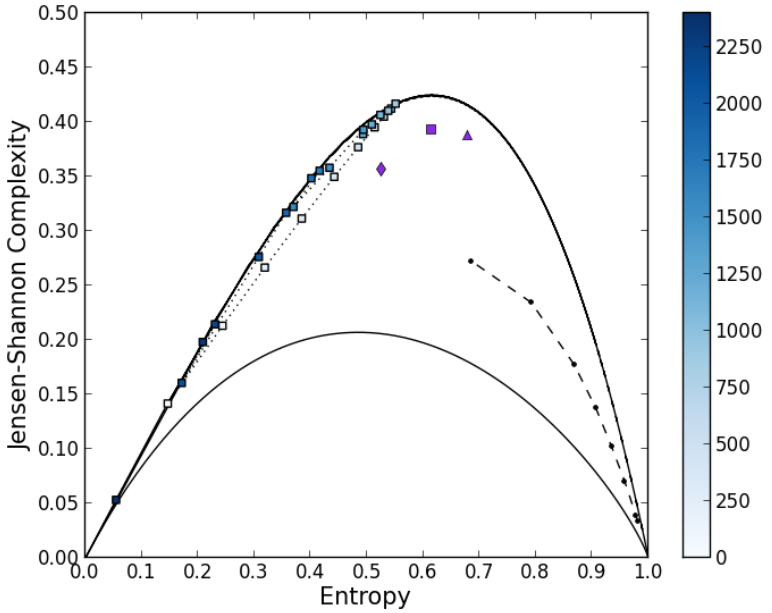

Figure 17: The $n = 5$ CH positions of the sine time series sampled at $d = 10^{-3}$ for a wider range of embedding delays, up to $\tau = 2500$.

number of available ordinal patterns $L - \tau(n-1)$ becomes very small, resulting in extremely low complexities and entropies just in virtue of the lack of statistics. The limit case is of course when no ordinal patterns of the requisite length are available, which occurs for this series at $\tau = 2500$. Thus it should be kept in mind that the behavior explored here is more an artifact of the finite range covered by a given time series and insufficient statistics than any inherent dynamics. These strange effects are of interest because insufficient statistics and limited domains are often encountered when working with experimental datasets.

The final study of the delay dependence of sine time series was to add noise to the time series analyzed, and look for the embedding delays required to move the CH position of the series near the noise-free range shown in Figure 15. This was done by adding a random number between 0 and 0.1 (a tenth of the amplitude) to each term in the $d = 10^{-3}$ series analyzed above. This can be thought of analogously to noise at a frequency comparable to an experimental sampling rate. The analogue of Figure 15(b) with this high-frequency noise is shown in Figure 18.

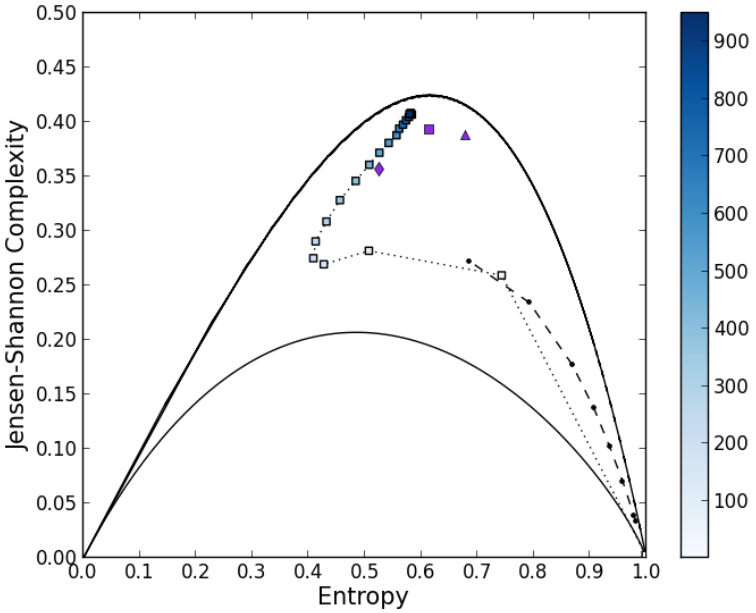

Figure 18: The $n = 5$ CH positions of a sine time series with high-frequency noise sampled at $d = 10^{-3}$ for a range of embedding delays up to 1000.

For delays of $\tau = 1$ and even $\tau = 50$, the series appears highly stochastic, with entropies and complexities comparable to fractional Brownian motion. It is not until delays of 150 or 200 that the CH positions becomes comparable to those of Figure 15(b). Interestingly, this delay is about as small compared to $\tau_c \approx 628$ as the delay at which the hook behavior appears is large compared to τ_c. This was anticipated, since delays less than but comparable to τ_c should be required to "see past" high-frequency noise. Said in other words, the ordinal range τnd at these delays is around $\pi/3$ or $\pi/4$, the same order of magnitude as the "inherent time scale" π. Even at larger delays, the entropies of the noise-added series remain slightly higher than without noise, but the point remains that the qualitative delay-dependent behavior is only accurately captured for delays comparable to τ_c when high-frequency noise is added to the time series.

Delay scans and insufficient statistics

By analyzing the CH position of a physical system over a range of embedding delays, details about the length scales on which different physical mechanisms

and dynamics are dominant might be extracted. However, as seen in the previous section, there are also effects such as insufficient statistics which artificially alter the CH position of a time series. Since time series from the SSX MHD wind tunnel consist only of 1300 values, understanding the artificial effects connected to insufficient statistics is of paramount importance.

Figure 19 explores the effect of large embedding delays on relatively short time series for all four datasets. Time series from each dataset were partitioned into sections of 1300 values, and the CH position calculated for each section separately and then averaged. The hope was that by holding the length of all time series analyzed constant and comparing their CH positions at high embedding delays, any striking commonalities which emerge across all four datasets could be attributed to the artificial effects of insufficient statistics. This would help determine the range of delays appropriate for reliable studies of SSX time series (reliable in the sense that changes in the CH position with embedding delay could be attributed primarily to physical sources instead of a lack of statistics). For reasons discussed in Section 4.2, $n = 5$ was chosen for this analysis. Each CH plane in Figure 19 includes the chaotic maps and fBm curve introduced earlier. Identical red curves, of the same basic shape as the maximum and minimum complexity bounds to the CH plane, were overlayed onto each of the subplots to ease comparison of high-embedding delay trajectories across datasets. These curves do not represent any CH computation, but merely a visual point of reference across subplots.

Each trajectory shown represents the (ensemble averaged) CH position as a function of the embedding delay, which is visually represented by a blue tone color scale. The first point in a given trajectory is the undelayed ($\tau = 1$) CH position, the next is the $\tau = 10$ position, then $\tau = 20$, and so on in steps of 10 over a range between $\tau = 1$ and $\tau = 200$. For the SSX delay scan in Figure 19(a), trajectories for both $\dot{B}$ (right side of the plane) and integrated B (left side) were calculated. Note that each point represents an ensemble average over approximately 40 shots at each of 8 helicity settings, as well as over the innermost 4 channels of the probe array and all three components of the magnetic field. Similarly, each point in the WIND trajectory in 19(b) consists of an ensemble average over the 1300 value sections and all three components of the magnetic field. Only the fast wind time series was used. The LAPD trajectory, shown in 19(d), represents averages over 1300 value sections of time series from 5 different runs. Finally, the liquid metal trajectory was calculated by averaging over 1300 value sections of the single magnetic time series available for this project.

The embedding delay trajectories for the four datasets naturally begin in different regions of the plane, with LAPD data at a high complexity and moderate

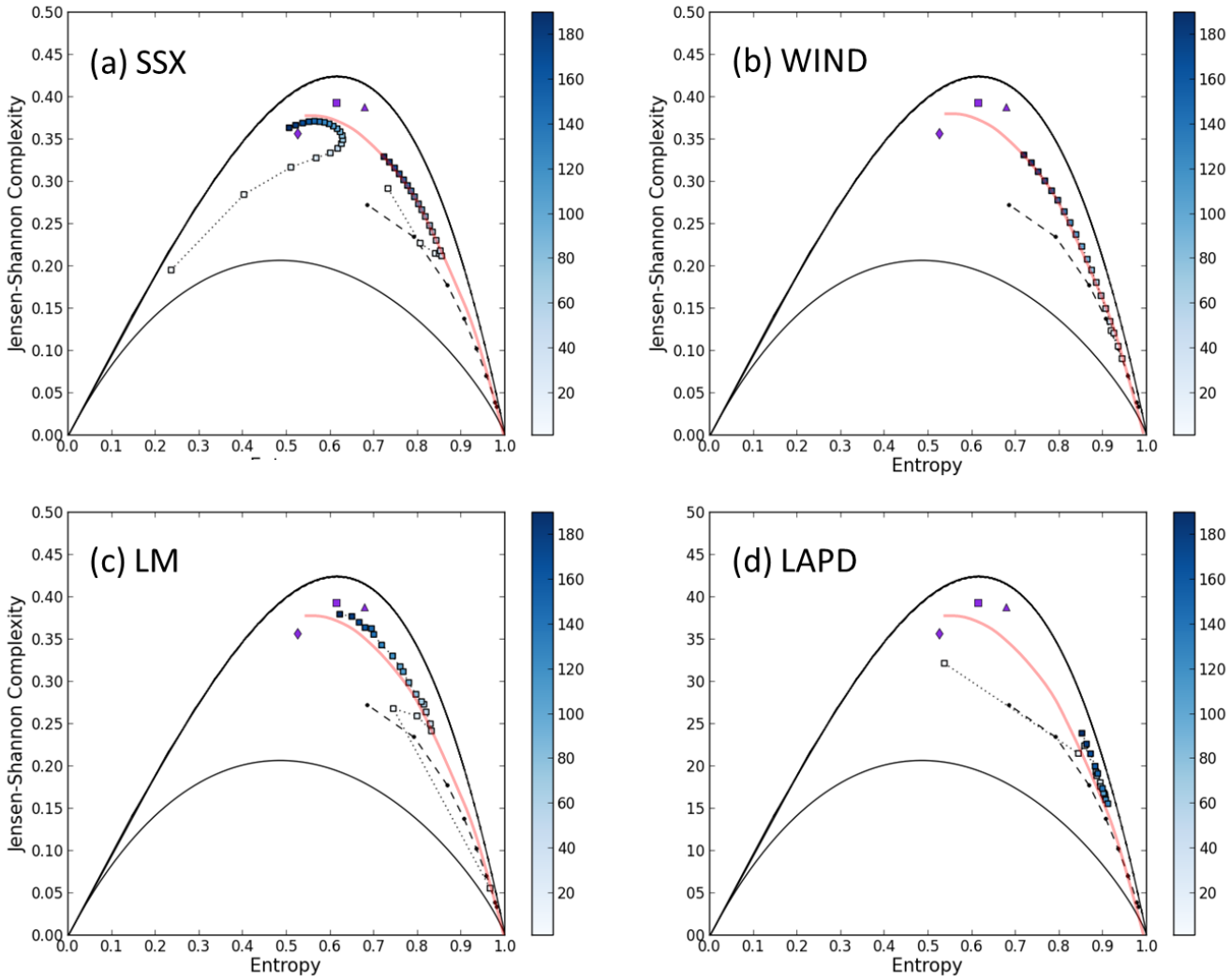

Figure 19: The $n = 5$ CH plane with embedding delay scans from $\tau = 1$ to $\tau = 200$ of (a) SSX $\dot{B}$ on the right hand side of the plane and B on the left, (b) fast solar wind B, (c) liquid metal B, and (d) LAPD I_{sat} time series, all of length $L = 1300$. Each point represents an average, either over multiple time series, 1300 value sections of single series, or both. The red curve was drawn to provide a common reference to aid comparison across subplots. Chaotic maps and a range of fBm points are also shown.

entropy, SSX $\dot{B}$ data at fairly high entropy and complexity, and solar wind and liquid metal data at extremely high entropies and low complexities. The significance of these systems occupying such disparate regions of the CH plane will be explored in later sections. What is of interest here is the overall CH trajectories followed by each system as the embedding delay τ is increased past the point where the number of $n = 5$ segments of every τth value in the series becomes insufficient to fill out the ordinal pattern probability distribution. In particular, note that for low embedding delays, there is a wide range of behaviors exhibited by these trajectories, while at high embedding delays, certain commonalities emerge. For example, for low to moderate delays, the CH position of LAPD data moves rapidly towards the high entropy and low complexity corner of the plane, while liquid metal CH positions increase in complexity and decrease in entropy. At high delays, all four trajectories execute a "left hook", followed by a monotonic decrease in entropy and increase in complexity, tracing comparable arcs towards the top of the CH plane. The fact that this high-delay trend occurs across all four systems suggests that it represents an artificial effect connected to a lack of statistics.

However, note that the "hook" occurs at different delays for each system. Finer delay scans indicated that the hook occurred much later for LAPD data, and earliest for WIND data. The table shown below displays the estimated embedding delay after which these ensemble averaged trajectories over 1300 value sections decrease in entropy and increase in complexity monotonically.

Dataset	τ_{hook}
SSX	34
WIND	6
LAPD	126
Liquid Metal	31

This variation in the value of τ_{hook} may be accounted for by the differing number of distinct ordinal permutations occurring in each time series. For example, Figure 20 shows the ordinal pattern probability distributions for $\tau = 1$ of both an $L = 1300$ solar wind fast stream time series and an $L = 1300$ LAPD time series. While 119 out 120 different length 5 ordinal patterns occur in the solar wind series, only 80 appear in the LAPD series. Recall that for a given delay τ, $L - \tau(n-1)$ ordinal patterns are available for analysis. Since L is not very long to begin with, we can think of the ordinal patterns from the solar wind series

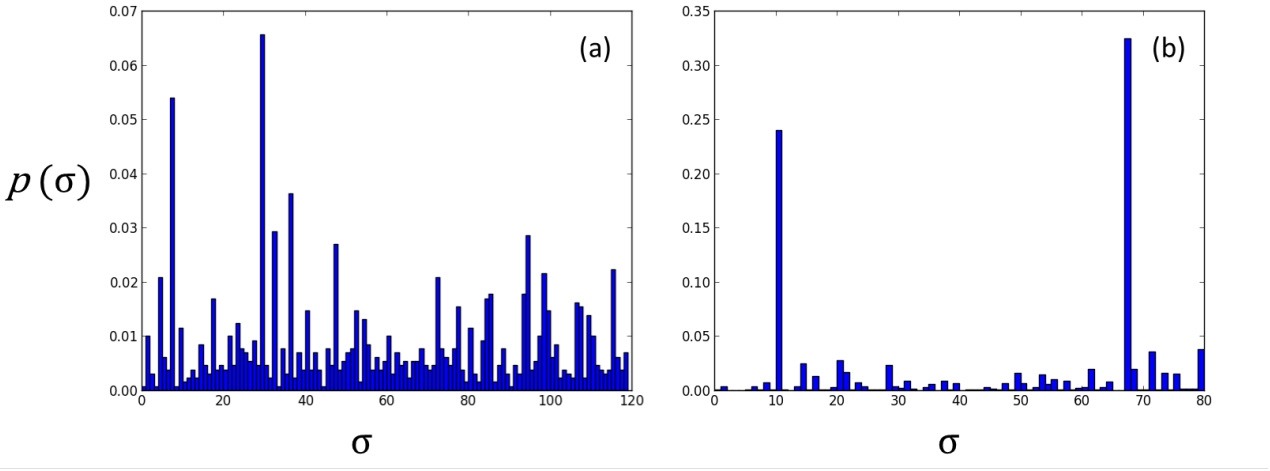

Figure 20: Ordinal pattern probability distributions for (a) fast stream B_x WIND data and (b) LAPD I_{sat} time series, each 1300 values in length, with no embedding delay. Note both the varying number of different permutations between the two datasets, as well as the difference in y-axis scales.

for $\tau = 1$ as already "spread thin" across the all 120 permutations accessible to the system at that time scale. The effect of insufficient statistics associated with large τ should be more significant for systems with broad distributions like the solar wind than for systems with more concentrated ordinal pattern distributions, simply because a histogram of counts from an inherently broad distribution is more likely to get accesible bins with no counts when the total number of counts is reduced. When fewer bins are getting counts, the system will start to look more complex, and the system will move up on the CH plane. Of course, differences in physical structure across length scales can also tend to increase or decrease the complexity and entropy as the embedding delay is increased. These trends might tend to push this artificial left hook behavior to earlier or later delays than would expected just by looking at the distributions at $\tau = 1$. In any case, generally speaking it makes sense that if the first portion of a system's trajectory is in a high entropy, low complexity region of the plane (i.e. the distribution of ordinal patterns is broader) then that trajectory would execute a left hook and move up the plane monotonically due to a lack of statistics at a lower embedding delay than a system which occupies a more complex region of the plan.

When the length of the time series considered is varied, most qualitative fea-

tures of the CH trajectories over scans of the embedding delay occur at approximately equal delays. However, the embedding delay at which the left hook effect described above occurs depends strongly on the length of the time series used, further indicating that these are artificial effects of insufficient statistics. For example, Figure 21 shows zoomed-in CH trajectories of different length time series from the liquid metal dataset, for embedding delays from $\tau = 1$ to 150 in steps of 1. 21(a) was generated by averaging the CH position over 1300 value sections of the original series, as in Figure 19, while (b) was generated by averaging over 2600 value sections. The qualitative behavior of these trajectories is quite similar. Both trajectories reach a local maximum in complexity near $\tau = 11$, which may indicate that some physical mechanism operating on time scales near $11 \times 1/f_{sample} = 11$ ms contributes additional structure to the magnetic fluctuations in the metal. On the other hand, while both exhibit the hook-like behavior, the hook occurs near $\tau = 72$ instead of $\tau = 31$ for the 2600 value sections. This suggests that unlike the local complexity maximum at $\tau = 11$, the hook does not reflect any physical structures.

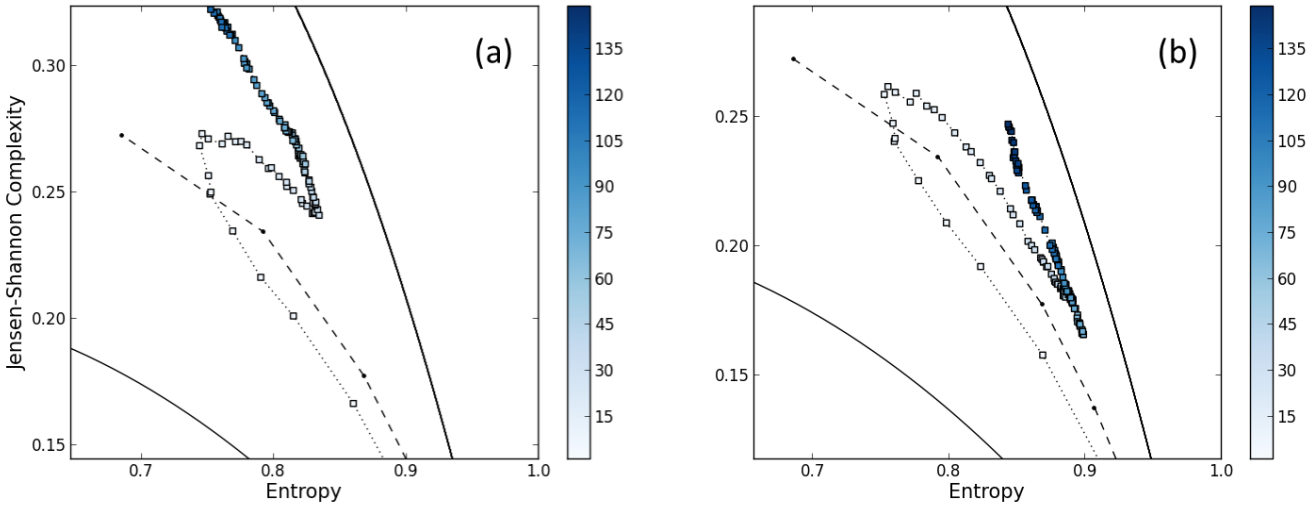

Figure 21: Close-ups of the trajectories of (a) 1300 value sections and (b) 2600 value sections of the liquid metal time series, for a scan of the embedding delay from $\tau = 1$ to 150 in steps of 1.

Similar observations can be made when comparing the results from partitioning the 5000 value LAPD time series into $L = 1300$ sections to those from analyzing

the full time series. Figure 22 shows close-ups of trajectories from these two cases over a range of delays from $\tau = 1$ to 100, again in steps of 1. The qualitative behavior is again similar over this range- both exhibit a local maxima in complexity near delays of $\tau = 10$, although for the 1300 value case the local minimum in complexity occurs at $\tau = 20$, vs $\tau = 14$ when the full time series is used. Like the local maximum in complexity for the liquid metal, this common feature occurring at similar delays could represent some additional structure on that time scale, in this case approximately 6 to 10 μs. On the other hand, while the hook behavior sets in near $\tau = 126$ for 1300 value sections of the LAPD dataset (just beyond the range shown in Figure 22), no hook is identifiable for the full length time series until after $\tau = 800$. Once again, these observations corroborate the hypothesis that a monotonic increase in complexity and decrease in entropy for delays which are large compared to the series length indicate that there are insufficient statistics available to accurately estimate the ordinal pattern probability distribution.

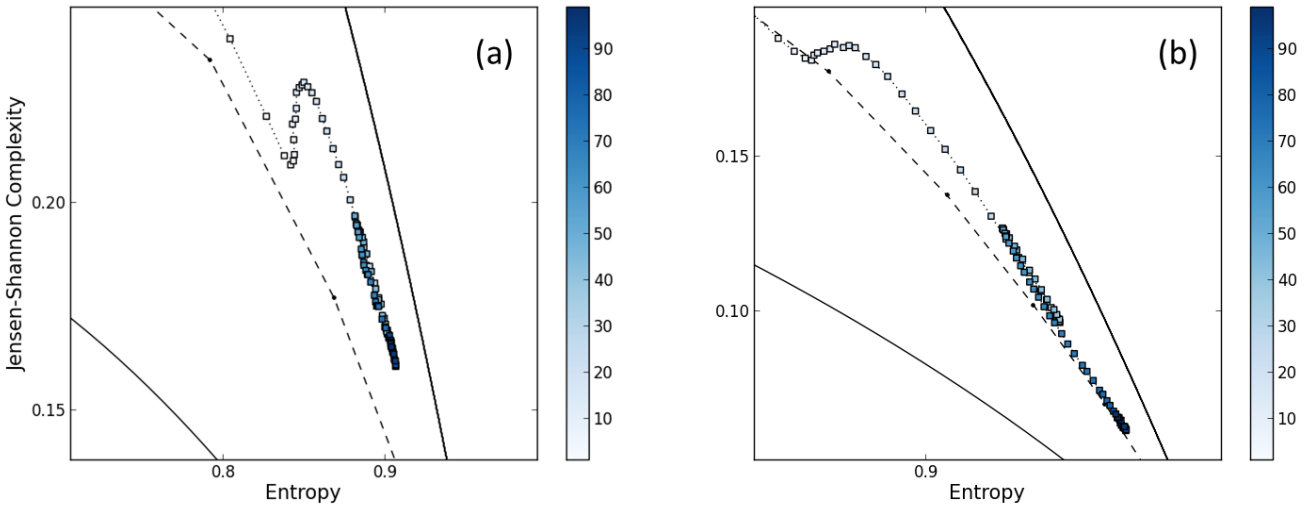

Figure 22: Close-ups of the trajectories of (a) 1300 value sections and (b) full length of the LAPD I_{sat} time series, averaged over 25 runs, for a scan of the embedding delay from $\tau = 1$ to 100 in steps of 1.

As we will see in Section 4.3, the left hook behavior may be less relevant for identifying the effects of insufficient statistics in longer time series, such as the full solar wind time series, which are hundreds of thousands of values long. However,

it seems reasonable to conclude that 1300 value SSX time series should not be analyzed with embedding delays past τ_{hook} if we are only interested in physical mechanisms. With this in mind, we now turn to what physical conclusions might be drawn from delay scans, and CH analysis more generally, of the SSX and WIND datasets.

Unfortunately, τ_h is fairly small for SSX time series, limiting the range of time scales which can be investigated. In particular, the complexity and entropy can only be calculated reliably for embedding delays corresponding to time scales between about $1/f_{sample} \approx 15$ ns and $1/f_{sample} \times \tau_h \approx 523$ ns. In frequency space, this corresponds to an upper bound on resolved frequencies between 65 MHz and about 2 MHz. With delay steps of 10, Figure 19(a) only provides a rough estimate of the delay dependence over this range. A finer scan of the embedding delay, in steps of 1, is shown over the same $\tau = 1$ to 100 range in Figure 23. The 15 ns to 523 ns range corresponds to the trajectory up to $\tau_h = 34$, corresponding to the turning point beyond which the trajectory enters a monotonic leftward arc. In this range, the average CH position of the dataset fluctuates rather rapidly, attaining its maximum complexity for the undelayed case, dropping immediately to its minimum complexity for $\tau = 2$, reaching its secondary maximum for $\tau = 8$, and subsequently working its way down and to the right. With such rapid fluctuations in complexity and entropy, it would be more difficult to identify a candidate time scale for some physical mechanism or mode than for, say, the simpler trajectory shown in Figure 21. It is interesting, however, that there is such a large increase in the stochasticity of the dataset at $\tau = 2$. This spike in stochasticity corresponds to a frequency of about 30 MHz. The SSX plasma gun is known to generate a high frequency noise mode at a frequency between 10 and 20 MHz. In a time domain, this high frequency mode corresponds to spans of about 133 ns, while each value in a $\tau = 2$ ordinal pattern for is about 31 ns apart. Thus it seems likely that the average position of SSX $\dot{B}$ signals moves to a more stochastic region of the CH plane at $\tau = 2$ due to the noise mode which is being near optimally resolved at that timescale.

4.4 Further Permutation Analysis - SSX

As can be seen in Figure 6 from Section 4.1, SSX magnetic frequency spectra follow a fairly steep, approximately -11/3 power law scaling for frequencies ranging from 1 MHz to about 10 MHz. The entire range of the CH trajectory in 23 from the secondary complexity maximum at $\tau = 8$ to the hook at $\tau = 34$ corresponds to frequencies between about 2 MHz and 8 MHz, so well within this steep power

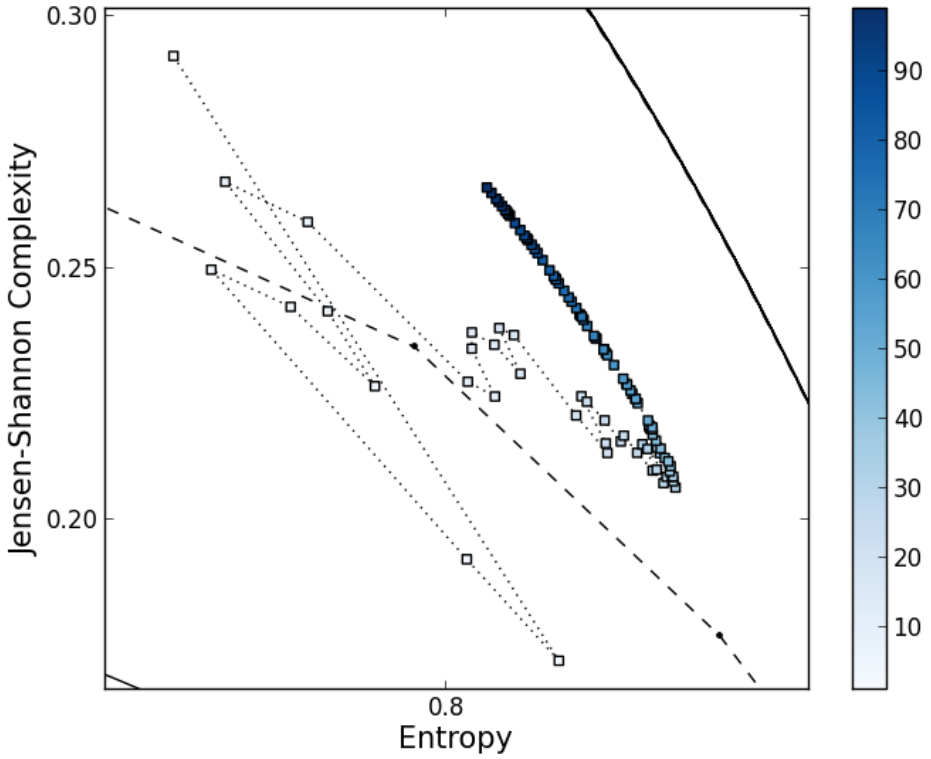

Figure 23: Close-up of the trajectory of helicity, channel, field component, and shot averaged SSX data for a scan of the embedding delay from $\tau = 1$ to 100 in steps of 1.

law range. In [25], it is suggested that the fact that SSX spectra exhibit this epoch of steeper power law scaling than the -5/3 of the solar wind could indicate a dissipative mechanism active in SSX but not the solar wind. As the embedding delay is increased in this range (i.e. as we move leftward in frequency space up towards the end of the -11/3 scaling regime), there seems to be a general trend towards greater stochasticity. If a dissipative mechanism is in fact responsible for the steeper power law scaling, it may also be connected to the changes in entropy and complexity over this $\tau = 8$ to $\tau = 34$ portion of the trajectory. Past this range, insufficient statistics prevent us from learning much about the overall dependence of the entropy and complexity of SSX magnetic fluctuations on time scale.

SSX CH spread for $\tau = 1$ and $\tau = 8$

In generating Figure 23, the CH position of the SSX dataset for a given embedding delay was found by averaging over components of the magnetic field, several channels, and numerous shots over a range of helicities. Recall that the magnetic helicity is a measure of the degree of "twistedness" of the plasma. Only the 40 to 60 μs stationary period of the plasma discharge was considered. We now turn to the dependence of the CH position of SSX time series on these various additional parameters. For simplicity, only two embedding delays are considered: $\tau = 1$ and $\tau = 8$. $\tau = 1$ is considered because the complexity is maximum at this delay, indicating that certain small-scale structures are being resolved which may be lost at larger delays.[8] However, a delay greater than 7 or so is required to avoid contamination from the high frequency noise mode discussed above. Thus the secondary complexity maximum at $\tau = 8$ is also used in many of the plots presented in this section. Note that this also keeps us well below the left hook at $\tau = 34$. As before, all CH planes with SSX data were generated using $n = 5$.

Figure 24 shows the overall spread of SSX data on the CH plane, for three different analysis windows and both $\tau = 1$ (left column) and $\tau = 8$ (right column). The first row displays the CH positions of all of the more than 15000 SSX time series in the dataset, analyzed between 40 and 60 μs after initial discharge. The blue circle indicates the average position, and the error bars the standard deviation horizontally and vertically from this average. The second row of plots was generated by analyzing the same dataset from 60 and 80 μs after discharge, by which time the plasma has developed into its helical minimum energy state and resistive dissipation has set in. Finally, the last row corresponds to an 80 and 100 μs analysis window, during which resistive dissipation has all but destroyed the magnetic field.

After the primary period of turbulent fluctuations is over and the plasma has relaxed, the average position of the data on the CH plane shifts to higher entropies and lower complexities, more characteristic of highly stochastic systems. The fluctuations in the magnetic field are becoming more random as it dies away due to the energy loss from resistive heating. Interestingly, this effect is either nonexistent or less pronounced when going from 40 to 60 μs to 60 to 80 μs for $\tau = 8$. Overall, with a $\tau = 8$ embedding delay the data is markedly more stochastic.

[8] There is nothing particularly special about the fact that this is the undelayed case- were the experimental sampling rate in the device faster, the maximum in complexity would likely occur at some larger delay.

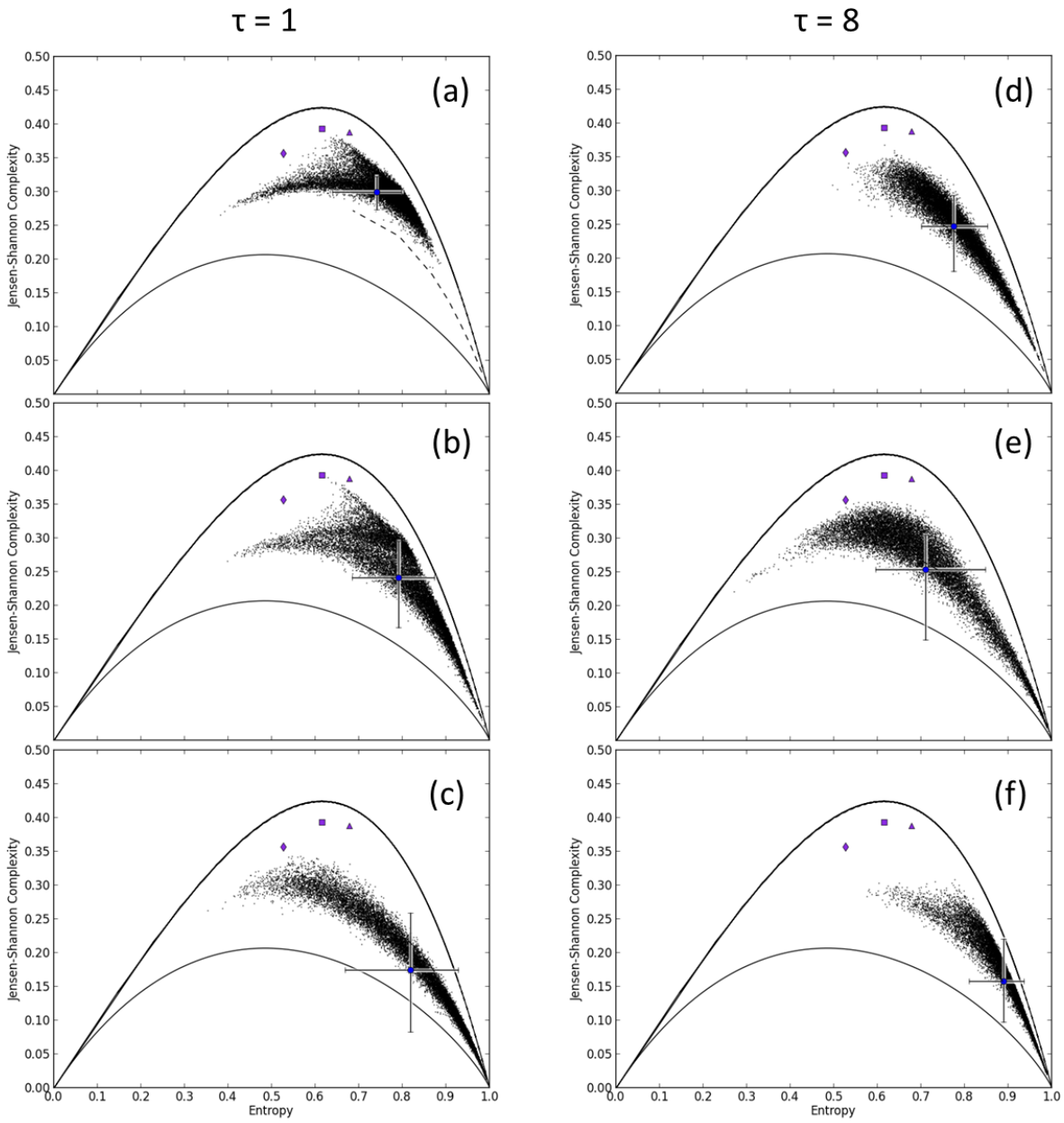

Figure 24: (a), (b), and (c) show the full spread of SSX data on the CH plane for $n = 5$ and $\tau = 1$, using analysis windows of 40 and 60 μs, 60 and 80 μs, and 80 and 100 μs, respectively. (d), (e), and (f) show the spread of data over the same three regimes calculated using an embedding delay of $\tau = 8$. Blue circles indicate average positions, and error bars indicate standard deviations above, below, to the right, and to the left of the mean.

Perhaps most striking about these plots are the large deviations from the mean, especially for later analysis windows. While some time series fall very far towards the stochastic limit of $H = 1$, $C = 0$, others lie near the chaotic maps, or reach towards the low entropy, low complexity region occupied by periodic functions. Two observations are in order here. First, much of the spread could be due to the shortness of each analysis window. If the stationary period in the discharge lasted longer than 20 μs, then time series would be longer than 1300 values and consequently more statistics would go into the calculation of the entropy and complexity. This would give us a more accurate picture of the dynamics at work, and potentially reduce the spread of the data on the CH plane. Secondly, even after we consider the effect of the length of SSX time series, there may be physical differences across helicity settings, probe positions, or components of the magnetic field which result in large deviations from the average CH position of the dataset as a whole. We turn next to a more detailed analysis of the effect these various parameters have on the CH position of SSX data.

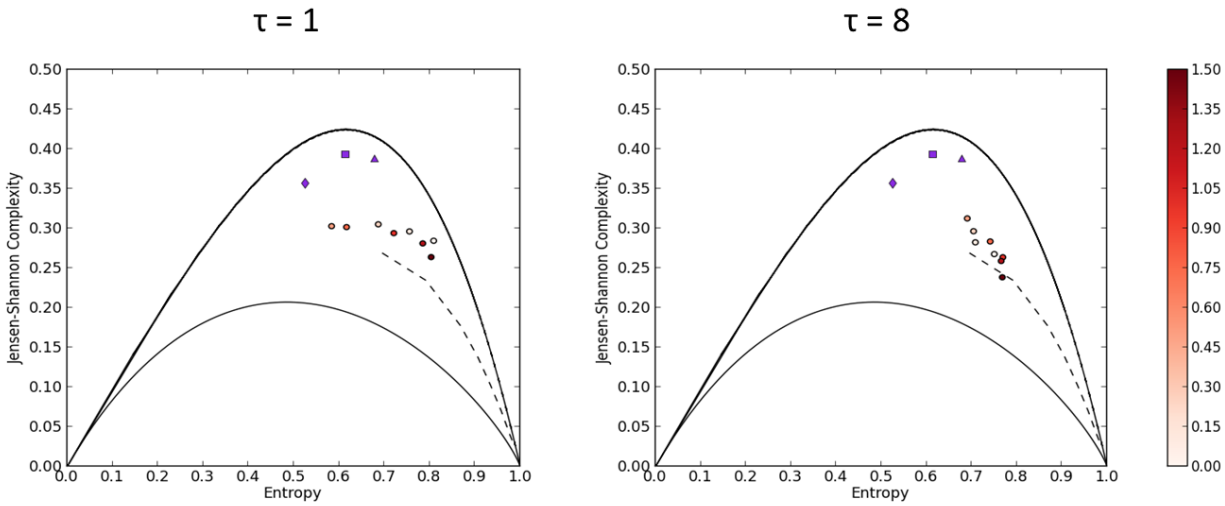

Figure 25: The CH positions of innermost probe channel SSX $\dot{B}$ time series, averaged over shots and components of the magnetic field, for eight different injected helicities. The color bar represents stuffing flux, in units of mWb.

Helicity Dependence

Figure 25 shows the shot and magnetic field component averaged CH position of SSX $\dot{B}$ data for eight different stuffing flux settings (0.0, 0.1, 0.25, 0.5, 0.75, 1.0, 1.25 and 1.5 mWb), corresponding to eight different helicities, or degrees of twist, of the injected spheromak. Each time series came from the innermost probe channel in the SSX device, and was analyzed only over the usual 40 to 60 μs window. There was little variation observed depending on which component of the magnetic field was used, so they were averaged over (and a dedicated section on field component dependence left out of this thesis). As in Figure 24, the results

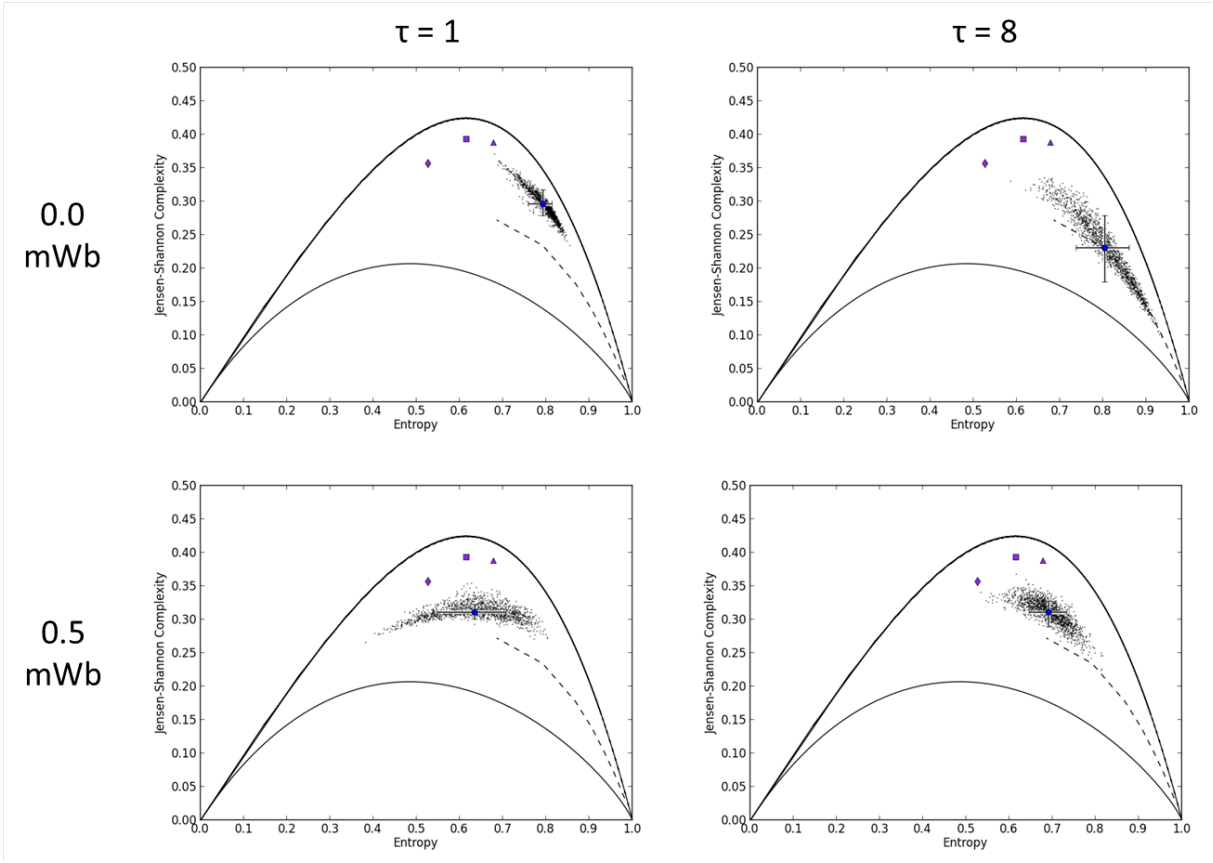

Figure 26: The CH positions of SSX time series for stuffing fluxes of 0.0 and 0.5 mWb, from all three magnetic field components of the 4 innermost probe channels, and all shots, with averages and standard deviations indicated. Not that results are shown for both $\tau = 1$ and $\tau = 8$.

are shown for both $\tau = 1$ and $\tau = 8$. For both embedding delays, there appears to be a loop-like path, or cycle, traced out on the CH plane as the helicity is varied. For $\tau = 1$, the entropy decreases for stuffing fluxes from 0.0 mWb to 0.5 mWb, and then increases from 0.5 mWb to 1.5 mWb, while the complexity remains more or less constant. For $\tau = 8$, the cycle is more vertical, i.e. it is the complexity that reaches an extremum at 0.5 mWb and takes on similar values for both the 0.0 and the 1.0 mWb stuffing flux settings. In any case, there appears to be a trend towards greater stochasticity in the SSX data the farther the stuffing flux applied in plasma gun during discharge is from approximately 0.5 mWb.

This effect is further illustrated in Figure 26, which shows the overall spread of data at the 0.0 and 0.5 mWb settings which was averaged over in creating Figure 25. The entire "cloud" of SSX points is closer to the upper-middle region of the plane at the 0.5 mWb stuffing flux setting, and farther down and/or to the right (i.e. more stochastic) for the 0.0 mWb setting. As for the plots of the full spread of the SSX dataset, using $\tau = 8$ instead of $\tau = 1$ seems to yield slightly more stochastic CH positions.

The question naturally arises: why a cyclic dependence on the magnetic helicity of the injected spheromak? One possible answer is that the minimum energy Taylor state of the plasma introduced in Section 2.3 has a magnetic helicity close to that generated by a 0.5 mWb stuffing flux shot. The spheromak can be thought of analogously to a stretched or compressed spring, with the compression representing magnetic helicity. If you only compress the spring a little, it will return to its equilibrium position without much oscillation, or with fewer dynamics, than if it is stretched or compressed a great deal. Similarly, if the injected spheromak has to "twist" around more in order to reach its equilibrium state, it will undergo more dynamics in the process, potentially yielding more stochastic magnetic fluctuations than if the injected helicity nearly matches the minimum energy helicity. Thus the CH position of the magnetic fluctuations will be farther down and to the right the farther the injected helicity is from that of the Taylor state. This is only a qualitative argument. Further work would be required to develop it into a working hypothesis about the relationship between injected helicity, the helicity of the relaxed state, and the CH position of the resulting magnetic fluctuations.

Position Dependence

The last source of spread in the CH position of SSX data which was analyzed is the radial position of the pick-up coil acquiring the data, or probe channel. The CH position of the data was averaged over helicity settings, shots, and components of

the magnetic field, and plotted as a function of probe channel for two embedding delays. These CH plots are shown in Figure 27. The color bar indicates the probe channel, with channel 0 representing the innermost radial position on the probe and 15 the outermost. For $\tau = 1$, no clear trend is evident, although when the embedding delay is $\tau = 8$, there appears to be a positive correlation between stochasticity and increasing radial distance. This dependence is quite possibly due to edge effects imposed by the chamber walls and ports, and along with helicity dependence probably accounts for much of the spread observed in the CH positions of SSX time series.

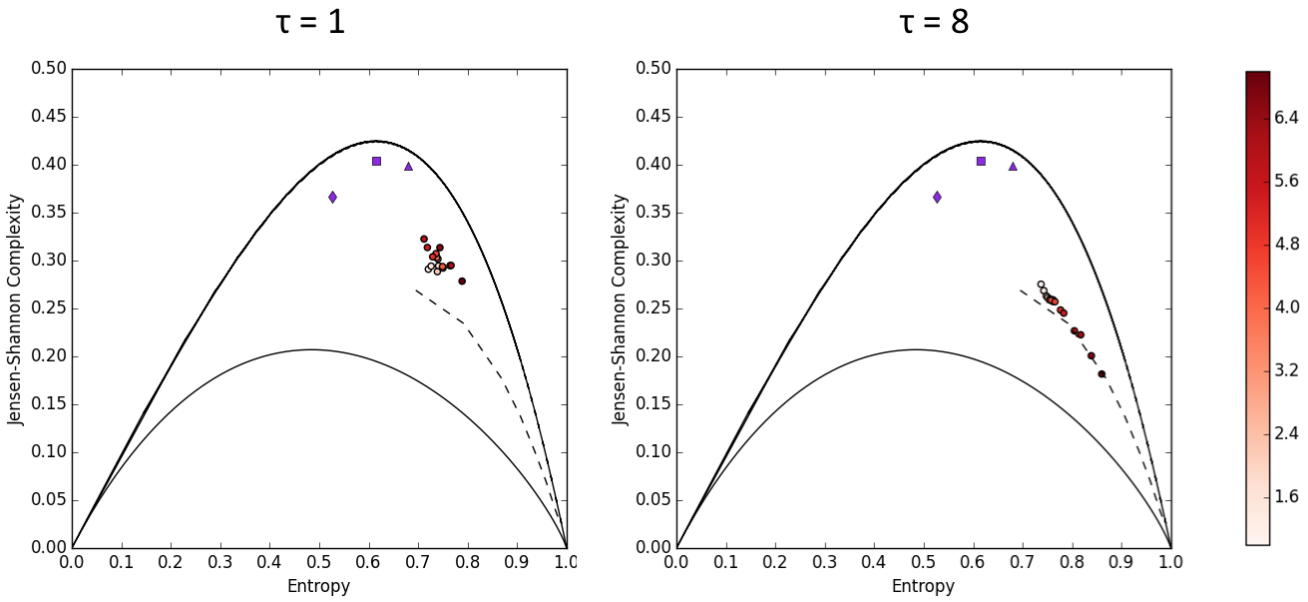

Figure 27: Dependence of CH position on probe channel (i.e. radial position in the wind tunnel). Each point was averaged over all shots at all helicity settings, as well as all 3 components of the magnetic field. Red tone color scale represents radial position in cm from the center of the device.

4.5 Further Permutation Analysis - WIND

The WIND dataset studied does not contain nearly as many different parameters as the SSX dataset, and displays much less spread in its CH position across time scales. Six time series are studied: three components each of the magnetic field in a fast and slow stream. Figure 28(a) shows the zoomed-in section of the $n = 5$ CH

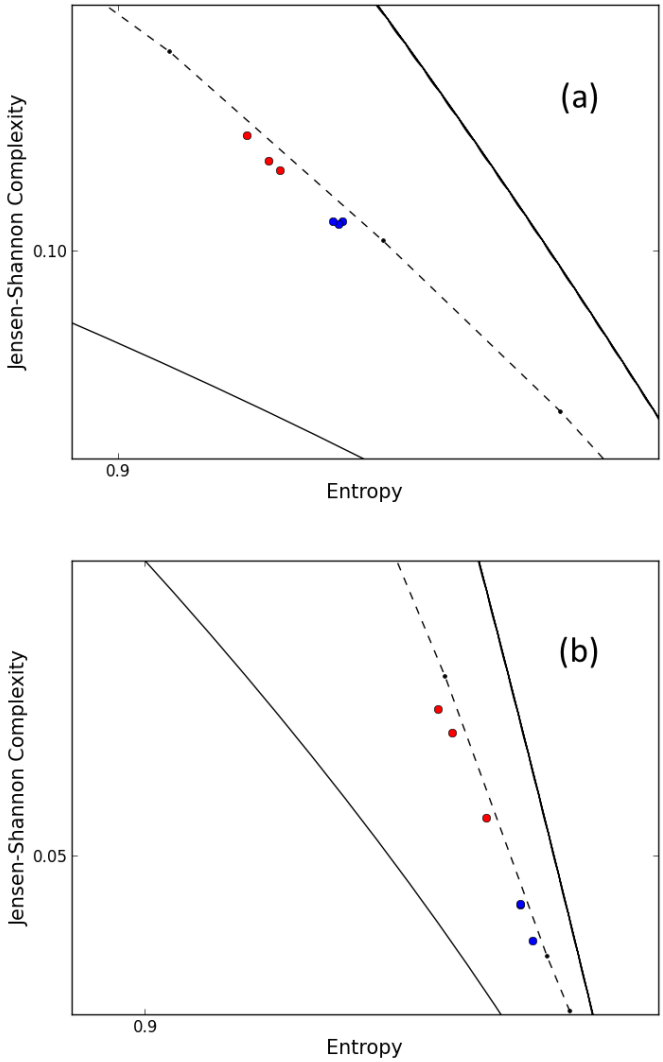

Figure 28: The CH positions of all three components of both fast stream (blue) and slow stream (red) magnetic fluctuations for $\tau = 1$ (a) and $\tau = 100$ (b)

plane showing all three components of the magnetic field for both fast and slow stream WIND data for $\tau = 1$. As for SSX, this embedding delay is of interest not because it is the sampling rate *per se*, but because it corresponds to a local maximum in the complexity, and thus maximally captures what correlated physical structures are present. The delay dependence of the dataset will be described in

detail later. For now only the dependence on magnetic field component and fast vs. slow stream for a single delay is considered.

Figure 28 shows fast stream data in blue, and slow stream data in red. There is little difference in CH position depending on which component of the magnetic field is analyzed, indicating a degree of isotropy. However, all three components of the fast stream signal are more entropic and have less complexity than any of the slow stream signals. The difference in complexity and entropy is only about 0.01, so it is not immediately clear that it reflects any physical feature of the two streams. However, the greater stochasticity of the fast stream does persist when larger time scales are analyzed. For example, Figure 28(b) shows the enlarged CH positions of these time series for $\tau = 100$, corresponding to a time scale of 5 minutes. One possible source for the higher entropy and lower complexity of the fast stream is that the higher incidence of uncorrelated Alfvénic fluctuations[9] in the fast wind contribute to a greater degree of stochasticity [52]. The greater stochasticity of the fast stream will be revisited later in the section.

CH trajectory for small τ

As discussed in Section 4.3, the effects of insufficient statistics seem to set in for smaller embedding delays for the highly stochastic solar wind time data than for SSX data. Consequently, the trajectory of the full wind time series for scans of the embedding delay is quite different from that of the 1300 value sections used to generate Figure 19. When the full time series is used, the solar wind data remains in a highly stochastic region of the CH plane over an enormous range of embedding delays, corresponding to time scales ranging from seconds to minutes and even hours. For example, Figure 29 shows the CH trajectory of the fast wind B_x time series over a range of time scales ranging from the 3 second sampling rate ($\tau = 1$) to 3 minutes ($\tau = 60$), for $n = 5$. There is a clear trend towards greater stochasticity in the direction of increasing embedding delays. The plot was not generated for a larger range of delays because the trajectory remains in the same corner of the plane all the way up through embedding delays corresponding to time steps of several hours.Like the fast wind, the slow wind time series displays general a trend towards decreased complexity and increased entropy over a wide range of embedding delays. Figure 30 shows a close-up of a delay scan of the slow wind data's $n = 5$ CH position over the same range of embedding delays as in Figure 29.

[9] Alfvén waves are low-frequency oscillations of ions along magnetic field lines, analogous to waves propagating in a string.

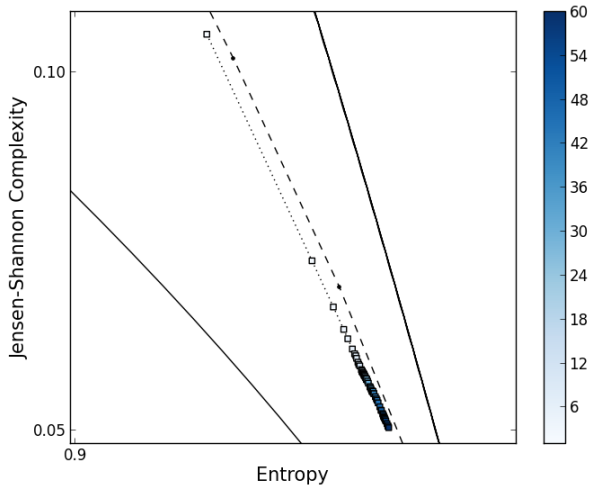

Figure 29: Embedding delay scan from $\tau = 1$ to $\tau = 60$ for the fast wind B_x time series. The color bar indicates the embedding delay used.

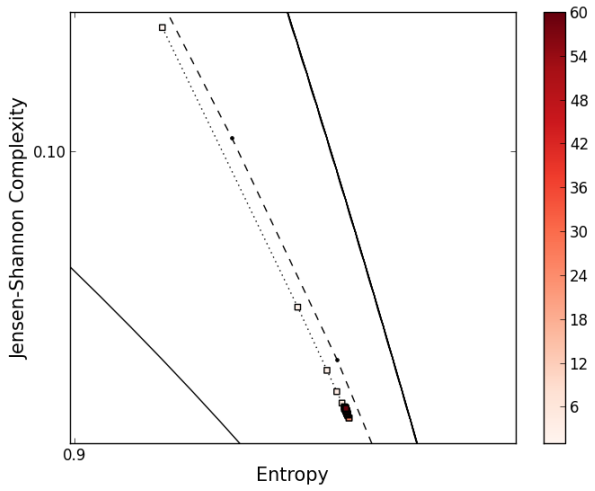

Figure 30: Magnetic field component-averaged positions of the slow stream WIND data over a range of embedding delays from $\tau = 1$ to $\tau = 60$ in steps of 1.

As will be examined in greater detail later, the slow wind data tends to have slightly higher complexity and lower entropy than the fast wind. Otherwise the scale-dependence appears quite similar.

What is the source of these increased entropies and reduced complexities at time scales of many seconds? As when examining the scale dependence of PE_{norm} and C_{JS} in the SSX device, it will be useful here supplement the CH analysis with frequency spectra for the data. Figure 31 shows the frequency spectrum of the fast wind B_x time series, with a -5/3 power law plotted for comparison. The minimum frequency plotted corresponds to approximately 1 day. Note that with a 3 s sampling rate, the dataset is already well into the inertial range, where energy cascade physics dominate. Time scales all the way up to a little over an hour are contained within this range, corresponding to embedding delays up to about $\tau = 1200$. Thus the trend towards high stochasticity may be connected to the physics of the energy cascade in the inertial range. As the embedding delay is increased, the maximum resolved frequency is effectively shifted deeper up into the inertial range, and thus farther from the dissipation scale. It would seem the result is that fewer physical structures are resolved, and that the fluctuations look more and more random.

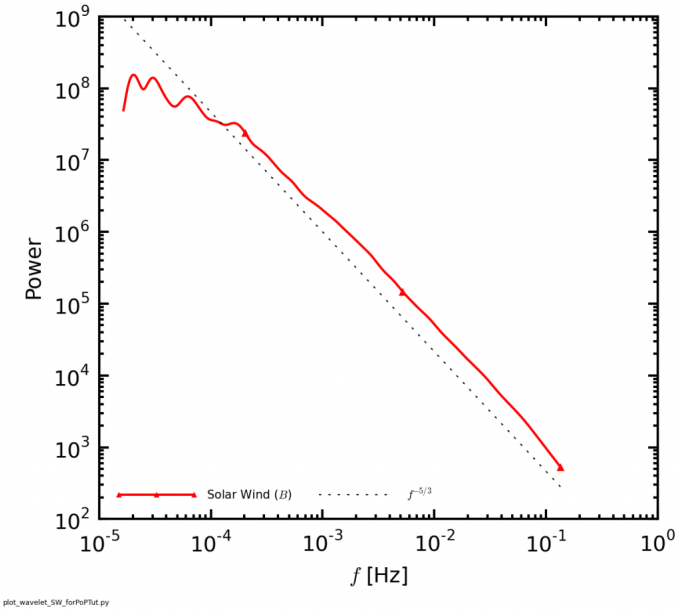

Figure 31: Frequency spectrum of WIND fast B_x time series, with -5/3 power law shown for comparison.

Additional structure may be present on the scale of a few days, which can be studied by conducting scans using larger values of the embedding delay.

CH trajectory for large τ

When much larger delays are used, the WIND data departs from the trend towards decreasing complexity and increasing entropy observed above. Figure 32 shows the results of a delay scan corresponding to time scales of about 1.6 to 2 days using the fast wind data. Note that steps of 400 were used in this scan of the embedding delay in order to reduce computation times. There is a general trend towards increased complexities for embedding delays of this magnitude, although finer scans indicate that this trend is far from monotonic. Furthermore, at least some of the trend is likely a result of insufficient statistics- for a delay of $\tau = 57200$, only a few hundred ordinal patterns go into the ordinal pattern distribution. However, the trend towards greater complexity appears to set in for delays of only around 50000, at which there are almost 30000 ordinal patterns entering into the permutation entropy calculation, so this trend is probably not completely artificial.

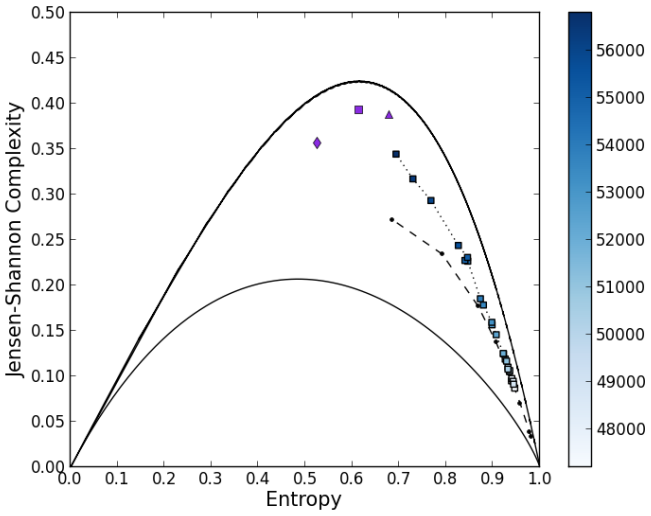

Figure 32: Magnetic field component-averaged positions of the fast stream WIND data over a range of embedding delays from $\tau = 47200$ to 57200 in steps of 400, corresponding to time scales ranging from about one and a half to two days.

The same embedding delay scan could not be calculated for the slow wind data, due to the shorter length of the time series. For the range of delays over which both fast and slow streams could be studied, their trajectories appear qualitatively similar. Interestingly, this similarity breaks down when larger embedding dimensions n are implemented, as discussed next.

Scans of the embedding delay for $n = 6$ and $n = 7$

As discussed in Section 4.2, when dealing with SSX data practical considerations limit the choice of embedding dimension to no more than $n = 5$, while for the solar wind we are free to use $n = 6$ and even $n = 7$. At a given embedding delay (i.e. timescale), additional structure may emerge when longer ordinal patterns are studied. With this in mind, the values of PE_{norm} and C_{JS} were calculated over a range of embedding delays for B_x solar wind time series, at $n = 5$,6, and 7. The results are presented in the scatter plots shown in Figure 33. Each column of scatter plots represents a different embedding dimension n. The first row of plots was generated using the slow wind time series, and the second the fast wind series.

As we might expect, the overall complexity of the solar wind dataset is greater, and the permutation entropy less, for larger embedding dimensions. Considering longer ordinal patterns captures structures which remain hidden for smaller dimensions of the embedding space. More interestingly, peaks in the complexity which are barely noticeable for $n = 5$ become pronounced when larger embedding dimensions are used. For example, for the slow stream series, there is an increase in complexity of less than 0.01 near $\tau = 7200$ (a time scale of about 6 hours) for $n = 5$. In the $n = 7$, scatter, the same peak occurs, but is over twice as large. This suggests a greater sensitivity to variations in structure across time scales for $n = 7$.

Perhaps most interestingly, while the general trend to higher entropies and lower complexities for time scales ranging from seconds to minutes holds up even at for $n = 6$ and $n = 7$ in the fast wind, the trend reverses for larger embedding dimensions in the slow wind time series. In other words, the difference between fast and slow streams becomes more pronounced when $n = 6$ or $n = 7$ is used, such that the slow wind actually exhibits greater structure at large time scales while the fast wind remains highly stochastic over a wide range of time scales. The slow wind originates from more complex magnetic topologies in the corona than the fast wind [13], and does not exhibit as many uncorrelated Alfvénic fluctuations [52], so these factors are possible sources of the additional complexity of the slow

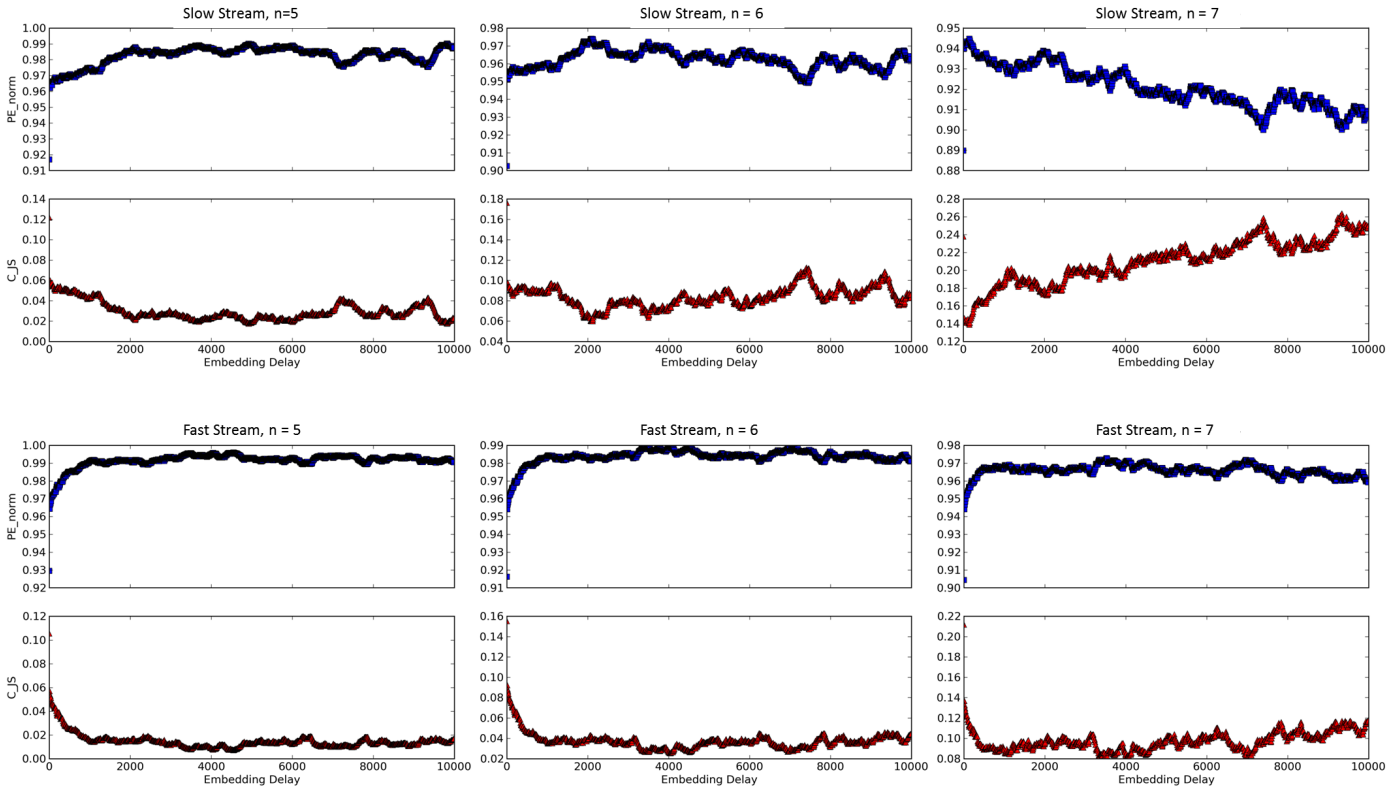

Figure 33: Scatter plots of the complexity and entropy of solar wind B_x time series for a range of embedding delays and embedding dimensions.

stream data. However, the particular character of the scale-dependence of the slow stream data will require further work to explain.

4.6 CH Plane Comparison of Turbulent Plasmas

The focus in the previous few sections has been on using the CH plane methodology to identify inherent time scales of a system, characterize the type of dynamics exhibited on particular scales, and identify the effects of various physical parameters on CH position within a given system. Much of the usefulness of this methodology lies in its generality. We can make further use of this generality by treating the CH plane as a common canvas on which to compare the dynamics of seemingly disparate systems. This has already been done to some degree here, using mathematical models as points of reference and comparison to identify stochastic, periodic, and chaotic like behavior. In this section, turbulent fluctuations in various plasmas are compared directly using the CH plane.

Figure 34 shows the $n = 5$ CH plane, with representative positions of turbulent SSX, WIND, and LAPD fluctuations, as well as the usual three chaotic maps, fBm curve, and a sine function ($d = 0.0001$, $L = 10^5$). Naturally, the positions of the three plasma systems reflect the dynamics dominant on a particular temporal scale (and where Taylor's hypothesis pertains, spatial scale). Given the practical limitations inherent in each dataset, the embedding delay was carefully chosen for each so as to provide a good point of comparison. For example, past work has suggested that LAPD fluctuations can be chaotic, due to the nonlinear interactions of particular modes in the plasma [2]. The sampling rate of the dataset studied here is just barely sufficient to capture the scale on which these modes exist, and thus adding an embedding delay makes the fluctuations appear far less complex than when no delay is used, as can be seen in Figure 19. Thus $\tau = 1$ was used here, in order to maximally capture the chaotic dynamics in LAPD I_{sat} fluctuations. Similarly, for the WIND dataset it was found that for $n = 5$, implementing an embedding delay only tended to reduce complexity and increase entropy unless extremely large scales on the order of several days were considered, thereby moving past the range on which turbulent cascade physics dominate. Thus $\tau = 1$ was chosen to calculate the CH position of WIND data shown in Figure 34. The choice of embedding delay for comparison across datasets was somewhat more difficult for SSX magnetic fluctuations. As was seen in Section 4.4, the length of SSX time series limits the range of time scales, or frequencies, which can be studied with the CH methodology. In particular, the range of frequencies over which SSX magnetic spectra display a relatively shallow power law scaling comparable

to the inertial range in solar wind turbulence is inaccessible. Only the steeper $-11/3$ power law region is accessible, where an additional dissipation mechanism not active in the solar wind could be dominant. SSX data also has an unwanted high-frequency noise mode near 10 or 20 MHz. With this limitations in mind, $\tau = 8$ was selected for comparison, thereby avoiding the high frequency mode and probing the dynamics in the somewhat mysterious $-11/3$ power law scaled region.

Figure 34 also includes separate points for fast and slow solar wind streams, SSX B and $\dot{B}$ fluctuations, and two helicity settings for each type of magnetic fluctuation. The associated error bars are intended to represent the typical degree of spread within a given system under a fixed experimental setting. They were calculated from the standard deviations in CH position across $\sim$ 40 shots, 3 magnetic field components, and the innermost 4 probe channels. Error bars for LAPD data, reflecting standard deviations across 25 runs, were not included, as they were approximately within the size of the marker. Solar wind points also do not include error bars, as they represent averages only over three components of the magnetic field, which display little difference in CH position.

Unsurprisingly, out of all the plasma systems considered, the LAPD edge fluctuations have entropies and complexities closest to those of the chaotic maps, with $H = 0.544$ and $C = 0.318$. SSX $\dot{B}$ fluctuations are considerable more entropic, especially for the 0.0 mWb stuffing flux setting. With $H = 0.688$ and $C = 0.311$, these fluctuations are actually occupy a region of the CH plane very near to fBm with slight positive correlations between increments. Although SSX B fluctuations exhibit similar complexities ($C = 0.288$ and $C = 0.314$ vs. $C = 0.311$ and $C = 0.247$), they are far less entropic than their $\dot{B}$ counterparts, even more so than the LAPD I_{sat} fluctuations. Whether this a general trend between variables and their derivatives, or an artificiality of the integration process is unclear. However, since the smoothing from the integration occurs on the scale of two or three consecutive values, with $\tau = 8$ it should not be having a very large effect.

Solar wind fluctuations are by far the most stochastic of all the plasma systems considered. With $H = 0.929$ and $C = 0.105$, the fast wind is even more stochastic than classical Brownian motion (fBm with Hurst exponent 1/2), in that it its distribution of ordinal patterns is even closer to uniform. The high degree of stochasticity makes sense when we consider that the solar wind turbulence is much more developed than SSX (for example, as noted earlier, the magnetic Reynolds number is approximately five orders of magnitude larger). Solar wind fluctuations develop for many days, and boundary conditions are imposed only by astrophysical bodies, while in SSX, fluctuations are confined to a space on the order of a few meters, and only last for tens of microseconds. Even so, there may

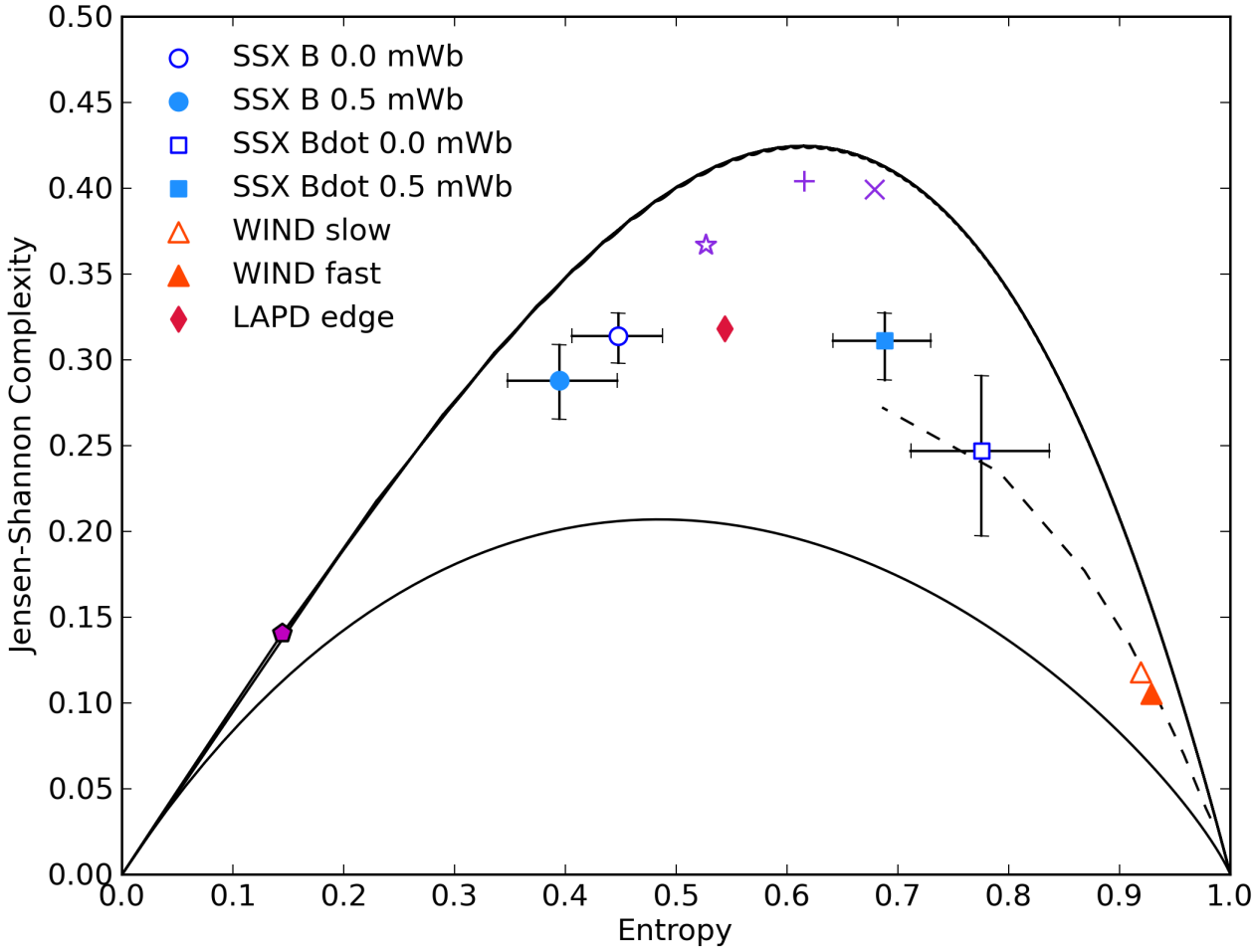

Figure 34: The $n = 5$ CH plane, with a variety of mathematical models and turbulent plasma fluctuations. Chaotic skew tent, Henon, and logistic maps are represented by the purple star, cross, and X markers, respectively. The pentagon marks the CH position of a discrete time series generated from the sine function. Fractional Brownian motion over a range of Hurst exponents is shown by the dashed black line.

be additional factors contributing to the ~ 0.2 difference in normalized entropies and complexities. In particular, the aforementioned practical limitations prevent us from comparing SSX and WIND fluctuations in strictly analogous frequency ranges. If the dissipation range is in general associated with more complex dynamics than the inertial range, then this could account for some of the discrepancy. Finer solar wind sampling or longer SSX signals would be required to compare across respective inertial and dissipation regimes, and see if there is a deeper connection between these two spectral regimes and the positions of the corresponding time series on the CH plane. Based on the findings of the previous section, there also seems to be a relationship between how "over" or "under" twisted the injected plasma is and how turbulent the resulting $\dot{B}$ fluctuations are. This could be taken advantage of to push SSX turbulence closer to solar wind turbulence on the CH plane.

So based on currently available datasets, it appears that the SSX plasma wind tunnel configuration would require some kind of modification to attain fully developed turbulence to the extent that is observed in the solar wind. However, if SSX plasma has turbulent regimes analogous to the inertial and dissipation ranges in the solar wind, we may just be comparing the two systems in different regimes. There may be fundamental differences between the complexity of magnetic fluctuations at dissipation scales and inertial range scales, and while the 3 s sampling rate of the WIND dataset restricts us to the inertial range of the solar wind, the short length of SSX time series restricts us to relatively small scales on which dissapative mechanism may dominate. To compare these plasmas over analogous turbulent regimes, we would need to either prolong the period of turbulent fluctuations in the SSX device with higher energy plasmas or study higher cadence solar wind data. Preliminary results on the difference in complexity between inertial and dissipation regimes using data from a satellite with a faster sampling rate are presented in Appendix A.

5 Conclusions

The CH methodology was developed as an multidisciplinary mathematical tool for understanding and distinguishing between different types of dynamics. The beauty of this tool lies in its generality- it can be applied to arbitrary time series, describing anything from stock markets and electrical impulses in the brain to magnetic fluctuations in the solar wind, and identifies dynamical commonalities between these seemingly unrelated phenomena. While the CH methodology has been applied to study plasmas in LAPD [3, 2], it remains far from established in the plasma physics community, and consequently its appropriate application is not well-understood. For example, the effects of series length on CH plane position, the conditions under which disparate systems can be compared based on the region they occupy in the CH plane, and the extent to which physical conclusions can be drawn by studying the complexity and entropy of a dataset are unclear. In the work presented here, these practical questions were explored and the CH methodology extended to solar wind turbulence, dynamical laboratory MHD turbulence, and liquid metal turbulence. While definitive answers remain elusive, there are a number of hypotheses, lessons, and tentative conclusions which can be drawn from this analysis:

(1) It should be kept in mind that the position of a system on the CH plane represents the complexity and entropy of that system at a particular time scale (or rather over a particular range of time scales) set by the choice of embedding delay and the sampling rate used to generate the time series. Thus plotting the CH position over a wide range of embedding delay most truthfully reflects the nature of the fluctuations in question.

   (a) Furthermore, plots of the complexity as a function of embedding delay seem to constitute a promising tool for identifying time scales of physical interest based on local extrema in the complexity.

(2) In addition to the oft-cited condition $L \gg n$ [51], intended to avoid the effects of insufficient statistics, the ordinal pattern probability distribution would ideally be constructed from a time series satisfying $L \gg \tau$ for the same reason. However, practically speaking this condition is often unattainable. The work presented here suggests that for relatively short time series, the embedding delay τ should at most take on the value for which the CH trajectory of the series begins a monotonic, leftward arc (i.e. the "left hook") across the CH plane. Recall that this upper bound, τ_h, appears to be smaller for highly stochastic time series with greater numbers of accessible ordinal patterns.

(3) Although the same term "turbulence" is used to describe fluctuations in many different plasma systems, including the solar wind, the LAPD edge plasma, and the SSX MHD wind tunnel device, the CH analysis presented here suggests these systems actually exhibit a great variety of different dynamics. Furthermore, in the spirit of (1), what type of dynamics (e.g. stochastic, chaotic, etc.) a given system exhibits is highly scale-dependent. This suggests the following refinements to our terminology:

   (a) Words like "stochastic" and "chaotic", already complicated by the fact that they are concepts borrowed from mathematics, should be qualified with reference to a particular temporal or spatial scale when used to describe physical systems.

   (b) The use of the word "turbulence" should perhaps be restricted or qualified, since some so-called turbulent systems are highly stochastic and others exhibit correlational structure characteristic of chaos.

(4) With these notes of caution in mind, magnetic fluctuations in the solar wind appear highly stochastic over a wide range of length scales, all within or below the inertial range in frequency space, while SSX $\dot{B}$ and integrated B signals span a wide region of the CH plane, depending on the time scale considered, the helicity of the injected plasma, the time after discharge, and perhaps the radial position in the tunnel. Overall SSX occupies an intermediate region of the CH plane, more complex than the WIND data, but also closer to fBm with positive correlations between increments than chaotic maps or LAPD edge fluctuations. The fact that the well-developed turbulence in the solar wind occupies a region associated with high stochasticity on the CH plane suggests that this may be a hallmark of well-developed turbulence, and thus that SSX fluctuations are a less developed form of turbulence.

(5) The CH plane methodology is sensitive to such dynamical differences as those associated with different injected helicities in SSX (using $n = 5$) and the variable degrees of structure vs. stochasticity in fast and slow stream plasmas (using larger embedding dimensions such as $n = 7$).

(6) Potential future applications of the CH methodology to plasma physics include:

   (a) Identifying time and/or length scales of physical import with no prior knowledge of these scales based on the dependence of complexity and entropy on embedding delay.

(b) Identifying when noisy-looking fluctuations in a plasma are the result of high degree of freedom, well-developed turbulence, and when they result from the non-linear interactions of coherent modes in the plasma, based on the proximity of the system to stochastic vs. chaotic models on the CH plane.

Item (6) would be especially interesting to explore in future work. In particular, do the time scales of greater complexity identified here in the various plasma datasets analyzed correspond to any important physical mechanisms, and with regard to (b), where do edge fluctuations in tokomaks and other fusion devices fall on the CH plane? Potentially interesting further research could also explore shorter time scales in the solar wind, capturing dynamics associated with dissipative mechanisms instead of just inertial energy cascades, and in the LAPD device, where the sampling rate of the dataset used here was just barely fast enough to capture the high-frequency modes associated with non-linear, chaotic interactions. For the SSX MHD wind tunnel device, this analysis has both indicated potential boundary condition limitations on our ability to accurately model astrophysical plasma turbulence in the lab, and opened the door to new techniques for studying, for example, the connection between turbulence and plasma helicity. In conclusion, measures of complexity based on ordinal patterns represent a promising new tool for the study of turbulent plasmas.

Acknowledgments

I would like to acknowledge Michael Brown and David Schaffner, for their continued mentorship and guidance. I am also grateful to Rob Wicks at NASA Goddard for connecting me to a WIND satellite dataset, and to the Swarthmore College Department of Physics and Astronomy for making this thesis research possible.

6 Appendix A: Cluster Dataset

The solar wind analysis presented in this thesis was limited to relatively large time scales by the 3 s sampling rate of the WIND dataset. In frequency space, the WIND data spans the inertial range of the frequency spectrum of the solar wind, where the $-5/3$ Kolmogorov scaling is dominant, without capturing much of the smaller-scale physics of the dissipation range. Preliminary CH analysis was also done on a second solar wind dataset from the Cluster II mission, which covers a greater portion of the dissipation range due to the faster sampling rate used. The results are presented in this appendix.

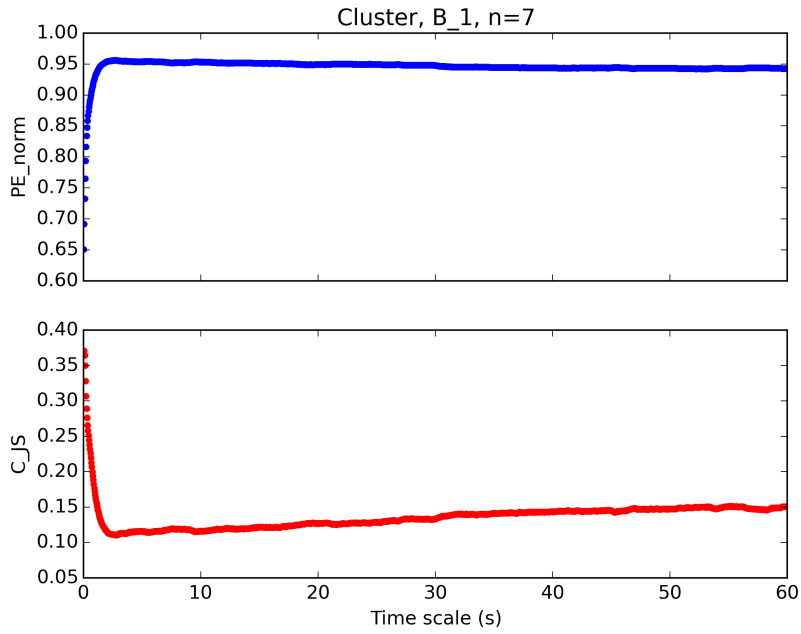

Figure 35: C_{JS} and PE_{norm} of the Cluster B_x time series as functions of time scale, in seconds ($\tau = 1$ to $\tau = 1500$). $n = 7$ was used.

Cluster II is a mission of four spacecraft arranged in a tetrahedral formation, launched primarily to study Earth's magnetosphere. However, the highly elliptical orbit of the spacecraft also allows them to make *in situ* measurements of the solar wind at a position roughly comparable to that of the WIND spacecraft. Cluster spacecraft acquire magnetic field measurements every 0.04 seconds, 75 times faster than WIND. Time series were analyzed from all four Cluster spacecraft, along the

same three orthogonal directions in which WIND acquires magnetic field time series. However, only the results for one Cluster spacecraft are presented, since there was little variation in complexity or entropy observed between spacecraft. Each time series from this spacecraft was 986, 091 values long, spanning a period of about 11 hours. This allowed the embedding delay to be selected from an large range using an $n = 7$ embedding dimension without concern regarding insufficient statistics. $n = 7$ was selected over smaller embedding dimensions since, as for the WIND datasets, trends in the complexity as a function of embedding dimension became more pronounced for larger embedding dimensions.

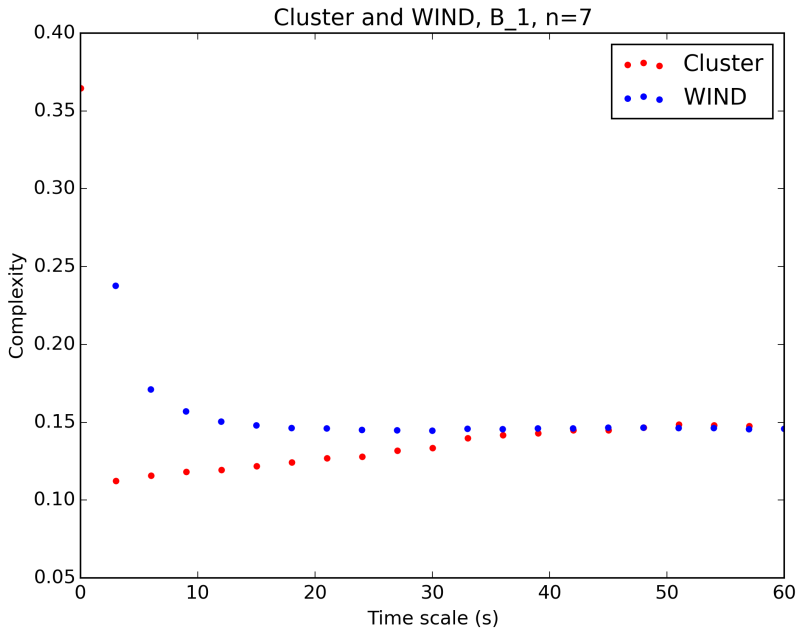

Figure 36: C_{JS} of both Cluster and slow WIND B_x time series over the same range of time scales as in 35, again for $n = 7$.

Figure 35 shows C_{JS} and PE_{norm} for the B_x time series [10], plotted as functions of time scale. For example, for an embedding delay of 100, the corresponding time scale is 0.04 s $\times 100 = 4$ s. The maximum embedding delay used was $\tau = 1500$, corresponding to a time scale of one minute. The complexity starts relatively

[10] As for the WIND dataset, magnetic field components are represented in GSE coordinates, with B_x aligned with the earth-sun direction, B_z the axis of the earth, and B_y orthogonal to the other two.

high at the time scale of the sampling rate, near $C_{JS} = 0.35$, but rapidly drops almost to $C_{JS} = 0.1$ as the time scale is increased to about 1 s. Over the same range of time scales, the entropy increases from about 0.65 to approximately 0.95. In frequency space, $t = 1$ s is right at the transition from dissipation to inertial range. For time scales larger than this transition, there is a gradual but steady increase in complexity and decrease in entropy.

A similar shift in complexity from the dissipation to inertial range is suggested by the WIND dataset, although the larger sampling rate only catches the tail end of the transition. Figure 36 plots the complexity of the slow WIND B_x data along with that of the Cluster B_x data, over the same range of time scales as in the previous figure. For ease of comparison, the Cluster data was aliased to have the same effective sampling rate as the WIND data (i.e. only every 75th Cluster point was plotted so as to have a 3 s interval between successive points from both datasets). The transition seems to be sharper for Cluster, but the same basic behavior is displayed by both datasets. Whether this difference is due to the different locations of the two spacecraft in the solar wind, the different filtering processes used to produce each dataset, or some other quirk of the time series is unclear. However, it seems clear that there is a rapid decrease in the complexity of magnetic fluctuations in the solar wind going from the dissipation dominated scale of 0.1 s into inertial range scales 1 s on.

The gradual, almost linear increase in complexity after the dissipation-inertial transition continues for time scales all the way up to 20 minutes, as shown in Figure 37 . The complexity is plotted for all three orthogonal magnetic field components, against the logarithm of the time scale to better display the transition occurring at small time scales. The same general trend appears for all three components of the magnetic field. However, the B_y series is more complex at large time scales, potentially indicating additional structures in fluctuations transverse to the earth-sun direction.

Finally, plotting the Cluster data on the CH plane with SSX and fBm reveals that at smaller time scales, solar wind turbulence is much more similar in entropy and complexity to SSX turbulence than was apparent using the WIND dataset. Figure 38 shows the Cluster B_x data over a range of time scales between 0.04 s and 2.0 on the $n = 5$ CH plane. The same chaotic map, fBm, and SSX $\dot{B}$ markers as in Figure 34 are included for comparison. Further work will be required to work out the details, but there appears to be a striking correspondence between the CH position of solar wind data in the dissipation-inertial range transition and fBm models with decreasing correlation between increments. At time scales in the dissipation range, the CH position of Cluster data also corresponds very

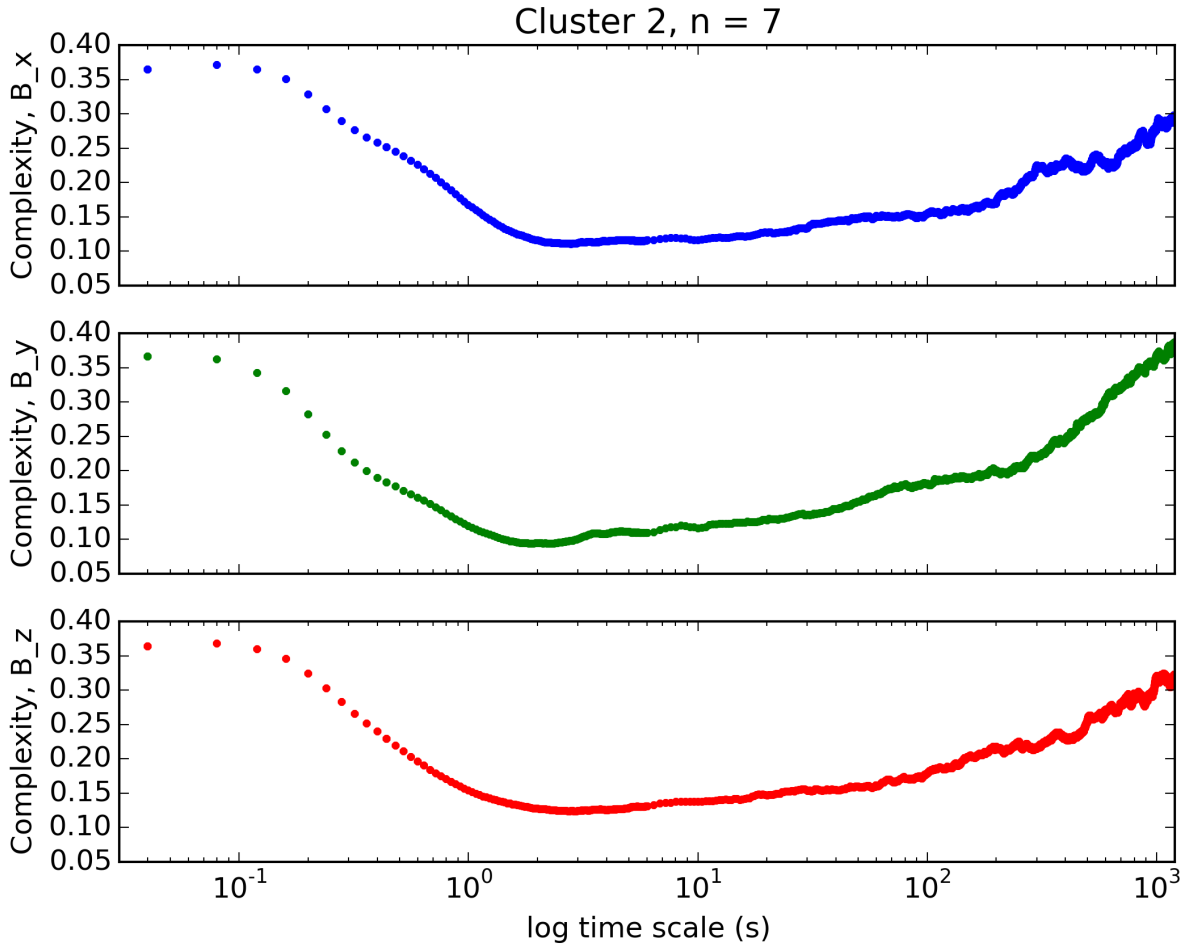

Figure 37: C_{JS} of the Cluster dataset for all three components of the magnetic field as a function of the logarithm of the time scale ($\tau = 1$ to $\tau = 30000$), using $n = 7$.

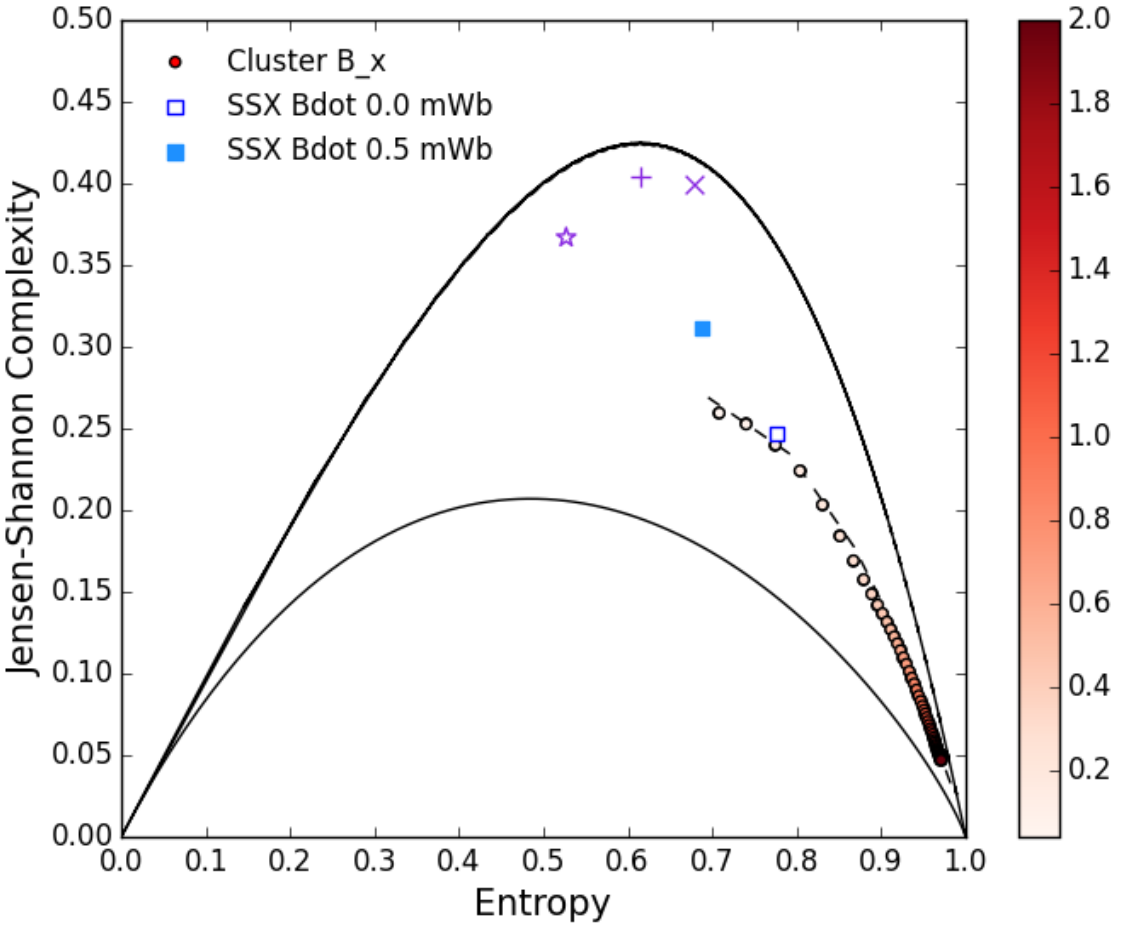

Figure 38: The $n = 5$ CH plane, with Cluster B_x data for a range of time scales between 0.04 s and 2.0 ($\tau = 1$ to $\tau = 50$), represented by the red color scale, in seconds. Chaotic skew tent, Henon, and logistic maps are represented by the purple star, cross, and X markers, respectively. Fractional Brownian motion over a range of Hurst exponents is shown by the dashed black line, barely visible beneath the Cluster data. The same two average SSX $\dot{B}$ positions from Figure 34 are also included for reference.

closely with that of 0.0 mWb SSX data, suggesting that the turbulent regime in SSX accessible using the CH methodology corresponds most closely to the dissipation range of solar wind turbulence. As mentioned in Section 4.6, the 100 μs lifetimes of SSX plasmas would need to be extended in some way to generate longer time series and thereby extend the CH analysis to larger time scales. In view of these results, it is likely that a similar transition in complexity to that from the dissipation to inertial ranges in the solar wind (Figures 35 and 36) would be observed.

7 Appendix B: the Chaotic-Stochastic Distinction

Although words like "chaotic" and "random" or are used interchangeably in everyday speech, the formal definitions for these words are very different.. Roughly speaking, chaos refers to the irregular behavior of solutions to certain nonlinear, deterministic equations. For example consider a simple iterated map, defined by

$$x_{n+1} = f(x_n),$$

where f is single-valued. Since this map is deterministic, given equal initial values the orbits traced out after some N iterations will always be identical. However, we say the dynamical system defined by this equation is chaotic if initial values x_0 arbitrarily close together (but not equal) result in exponentially divergent orbits. Time series generated from such maps often appear random. However, when the state space of solutions to chaotic systems of equations are studied, it is often found that the seemingly random fluctuations actually relax to complicated but bounded attractors, which often exhibit fractal structure.

In physical systems, the equations describing the dynamics can be chaotic in this formal, mathematical sense. For example, the double pendulum equations of motion are chaotic at certain energies, as are the equations describing voltage in a Chua circuit. However, even when the exact equations of motion are unknown, chaotic-like behavior can be identified based on statistical analyses of time series collected from the system. So even if true mathematical chaos is not strictly speaking present, we can describe, say, a time series of magnetic fluctuations in a plasma as chaotic in this approximate sense. For the purposes of convenience, "chaotic" is used in this thesis to refer to both systems exhibiting chaos in the true, mathematical sense and those physical systems which bear the statistical hallmarks of chaos.

While the mathematical definition of chaos applies only to deterministic systems, stochastic systems are inherently probabilistic. If a dynamical system is stochastic, not only will arbitrarily close initial values generally yield different orbits, but identical initial values will result in different orbits. Thus "stochastic" is generally synonymous with "random". [11] While physical systems are stochastic on a quantum mechanical level, on a macroscopic scale where deterministic

[11] It might be argued that while random implies stochastic, the reverse is not quite accurate. For example, while an idealized coin toss is both stochastic and perfectly random, tossing a coin weighted to land heads 90% of the time is certainly a stochastic process, but not perfectly random.

models hold to a high degree of accuracy the concept may appear inappropriate. However, in turbulent systems where the number of (approximately) deterministic interactions is so great that only a statistical description is available, we observe dynamics which are almost indistinguishable from those of truly stochastic models. In such circumstances, as for the chaotic analogue, the term "stochastic" has been used in lieu of the more unwieldy "stochastic-like".

Bibliography

[1] P. J. Weck, D. A. Schaffner, M. R. Brown, and R. T. Wicks, "Permutation entropy and statistical complexity analysis of turbulence in laboratory plasmas and the solar wind," *Phys. Rev. E*, vol. 91, p. 023101, Feb 2015.

[2] J. E. Maggs and G. J. Morales, "Permutation entropy analysis of temperature fluctuations from a basic electron heat transport experiment," *Plasma Physics and Controlled Fusion*, vol. 55, no. 8, p. 085015, 2013.

[3] W. Gekelman, B. V. Compernolle, T. DeHaas, and S. Vincena, "Chaos in magnetic flux ropes," *Plasma Physics and Controlled Fusion*, vol. 56, no. 6, p. 064002, 2014.

[4] W. McComb, *The Physics of Fluid Turbulence*. Clarendon Press, 1991.

[5] U. Frisch, *Turbulence: the legacy of A.N. Kolmogorov*. Cambridge University Press, 1995.

[6] J. Jimnez, "The contributions of a. n. kolmogorov to the theory of turbulence," *Arbor : Ciencia, Pensamiento y Cultura*, 2004.

[7] G. I. Taylor, "The spectrum of turbulence," in *Proceedings of the Royal Society of London A: Mathematical, Physical and Engineering Sciences*, vol. 164, pp. 476–490, The Royal Society, 1938.

[8] S. G. Saddoughi and S. V. Veeravalli, "Local isotropy in turbulent boundary layers at high reynolds number," *Journal of Fluid Mechanics*, vol. 268, pp. 333–372, 6 1994.

[9] V. Bothmer and I. A. Daglis, *Space Weather -Physics and Effects*. Springer, 2006.

[10] L. Biermann, "Kometenschweife und solare Korpuskularstrahlung," vol. 29, p. 274, 1951.

[11] W. H. Matthaeus and M. L. Goldstein, "Measurement of the rugged invariants of magnetohydrodynamic turbulence in the solar wind," *Journal of Geophysical Research: Space Physics*, vol. 87, no. A8, pp. 6011–6028, 1982.

[12] W. H. Matthaeus and M. L. Goldstein, "Stationarity of magnetohydrodynamic fluctuations in the solar wind," *Journal of Geophysical Research: Space Physics*, vol. 87, no. A12, pp. 10347–10354, 1982.

[13] C. Tu, E. Marsch, and H. Rosenbauerr, "The dependence of mhd turbulence spectra on the inner solar wind stream structure near solar minimum," *Geophys. Res. Lett.*, vol. 17, pp. 283–286.

[14] R. Bruno and V. Carbone., "The solar wind as a turbulence laboratory," *Living Rev Solar Phys*, vol. 10, 2013.

[15] F. Sahraoui, M. L. Goldstein, G. Belmont, P. Canu, and L. Rezeau, "Three dimensional anisotropic k spectra of turbulence at subproton scales in the solar wind," *Physical review letters*, vol. 105, no. 13, p. 131101, 2010.

[16] F. Sahraoui, M. Goldstein, P. Robert, and Y. Khotyaintsev, "Evidence of a cascade and dissipation of solar-wind turbulence at the electron gyroscale," *Phys. Rev. Lett.*, vol. 102, p. 231102, Jun 2009.

[17] B. T. Tsurutani and E. J. Smith, "Interplanetary discontinuities: Temporal variations and the radial gradient from 1 to 8.5 au," *Journal of Geophysical Research: Space Physics (1978–2012)*, vol. 84, no. A6, pp. 2773–2787, 1979.

[18] L. Sorriso-Valvo, V. Carbone, P. Veltri, G. Consolini, and R. Bruno, "Intermittency in the solar wind turbulence through probability distribution functions of fluctuations," *Geophysical Research Letters*, vol. 26, no. 13, pp. 1801–1804, 1999.

[19] A. Greco, P. Chuychai, W. Matthaeus, S. Servidio, and P. Dmitruk, "Intermittent mhd structures and classical discontinuities," *Geophysical Research Letters*, vol. 35, no. 19, 2008.

[20] A. Greco, W. H. Matthaeus, S. Servidio, P. Chuychai, and P. Dmitruk, "Statistical analysis of discontinuities in solar wind ace data and comparison with intermittent mhd turbulence," *The Astrophysical Journal Letters*, vol. 691, no. 2, p. L111, 2009.

[21] C. G. R. Geddes, T. W. Kornack, and M. R. Brown, "Scaling studies of spheromak formation and equilibrium," *Physics of Plasmas (1994-present)*, vol. 5, no. 4, 1998.

[22] T. Gray, M. R. Brown, and D. Dandurand, "Observation of a relaxed plasma state in a quasi-infinite cylinder," *Phys. Rev. Lett.*, vol. 110, p. 085002, Feb 2013.

[23] D. A. Schaffner, A. Wan, and M. R. Brown, "Observation of turbulent intermittency scaling with magnetic helicity in an mhd plasma wind tunnel," *Phys. Rev. Lett.*, vol. 112, p. 165001, Apr 2014.

[24] D. A. Schaffner, M. R. Brown, and V. S. Lukin, "Temporal and spatial turbulent spectra of mhd plasma and an observation of variance anisotropy," *The Astrophysical Journal*, vol. 790, no. 2, p. 126, 2014.

[25] D. Schaffner, V. S. Lukin, A. Wan, and M. R. Brown, "Turbulence analysis of an experimental flux rope plasma," *Plasma Physics and Controlled Fusion*, vol. 56, p. 20, 2014.

[26] M. R. Brown and D. A. Schaffner, "Laboratory sources of turbulent plasma: a unique mhd plasma wind tunnel," *Plasma Sources Science and Technology*, vol. 23, no. 6, p. 063001, 2014.

[27] D. P. Feldman and J. P. Crutchfield, "Measures of statistical complexity: Why?," *Physics Letters A*, vol. 238, no. 45, pp. 244 – 252, 1998.

[28] R. López-Ruiz, H. Mancini, and X. Calbet, "A statistical measure of complexity," *Physics Letters A*, vol. 209, no. 56, pp. 321 – 326, 1995.

[29] M. Zanin, L. Zunino, O. A. Rosso, and D. Papo, "Permutation entropy and its main biomedical and econophysics applications: A review," *Entropy*, vol. 14, no. 8, pp. 1553–1577, 2012.

[30] C. Bandt and B. Pompe, "Permutation entropy: A natural complexity measure for time series," *Phys. Rev. Lett.*, vol. 88, p. 174102, Apr 2002.

[31] J. M. Amigo, *Permutation complexity in dynamical systems : ordinal patterns, permutation entropy and all that*. Springer, 2010.

[32] C. Bandt, "Ordinal time series analysis," *Ecological Modelling*, vol. 182, no. 34, pp. 229 – 238, 2005. Scaling, fractals and diversity in soils and ecohydrology.

[33] P. Lamberti, M. Martin, A. Plastino, and O. Rosso, "Intensive entropic nontriviality measure," *Physica A: Statistical Mechanics and its Applications*, vol. 334, no. 12, pp. 119 – 131, 2004.

[34] O. A. Rosso, H. A. Larrondo, M. T. Martin, A. Plastino, and M. A. Fuentes, "Distinguishing noise from chaos," *Phys. Rev. Lett.*, vol. 99, p. 154102, Oct 2007.

[35] J. M. Amigó, S. Zambrano, and M. A. F. Sanjuán, "Combinatorial detection of determinism in noisy time series," *EPL (Europhysics Letters)*, vol. 83, no. 6, p. 60005, 2008.

[36] X. Li, G. Ouyang, and D. A. Richards, "Predictability analysis of absence seizures with permutation entropy," *Epilepsy Research*, vol. 77, no. 1, pp. 70 – 74, 2007.

[37] E. Olofsen, J. W. Sleigh, and A. Dahan, "Permutation entropy of the electroencephalogram: a measure of anaesthetic drug effect," *British Journal of Anaesthesia*, vol. 101, no. 6, pp. 810–821, 2008.

[38] D. Li, X. Li, Z. Liang, L. J. Voss, and J. W. Sleigh, "Multiscale permutation entropy analysis of eeg recordings during sevoflurane anesthesia," *Journal of Neural Engineering*, vol. 7, no. 4, p. 046010, 2010.

[39] A. F. Bariviera, L. Zunino, M. B. Guercio, L. B. Martinez, and O. A. Rosso, "Efficiency and credit ratings: a permutation-information-theory analysis," *Journal of Statistical Mechanics: Theory and Experiment*, vol. 2013, no. 08, p. P08007, 2013.

[40] L. Zunino, B. M. Tabak, F. Serinaldi, M. Zanin, D. G. Prez, and O. A. Rosso, "Commodity predictability analysis with a permutation information theory approach," *Physica A: Statistical Mechanics and its Applications*, vol. 390, no. 5, pp. 876 – 890, 2011.

[41] M. Soriano, L. Zunino, O. Rosso, I. Fischer, and C. Mirasso, "Time scales of a chaotic semiconductor laser with optical feedback under the lens of a permutation information analysis," *Quantum Electronics, IEEE Journal of*, vol. 47, pp. 252–261, Feb 2011.

[42] P. M. Saco, L. C. Carpi, A. Figliola, E. Serrano, and O. A. Rosso, "Entropy analysis of the dynamics of el niño/southern oscillation during the holocene," *Physica A: Statistical Mechanics and its Applications*, vol. 389, no. 21, pp. 5022 – 5027, 2010.

[43] X. Calbet and R. López-Ruiz, "Tendency towards maximum complexity in a nonequilibrium isolated system," *Phys. Rev. E*, vol. 63, p. 066116, May 2001.

[44] H. Pfister, W. Gekelman, J. Bamber, D. Leneman, and Z. Lucky, "A fully threedimensionalmovable, 10mlong, remotely controllable probe drive for a plasma discharge device," *Review of Scientific Instruments*, vol. 62, no. 12, 1991.

[45] D. Schaffner, T. A. Carter, G. D. Rossi, D. S. Guice, J. E. Maggs, S. Vincena, and B. Friedman *Phys. Rev. Lett.*, vol. 109, p. 135002, 2012.

[46] J. E. Maggs and G. J. Morales, "Magnetic fluctuations associated with field-aligned striations," *Geophysical Research Letters*, vol. 23, no. 6, pp. 633–636, 1996.

[47] J. E. Maggs and G. J. Morales, "Exponential power spectra, deterministic chaos and lorentzian pulses in plasma edge dynamics," *Plasma Physics and Controlled Fusion*, vol. 54, no. 12, p. 124041, 2012.

[48] R. K. C. J. M.D. Nornberg, E.J. Spence and C. Forest, "Measurements of the magnetic field induced by a turbulent flow of liquid metal," *Phys. Plasmas*, vol. 13, 2006.

[49] L. Zunino, M. Zanin, B. M. Tabak, D. G. Prez, and O. A. Rosso, "Complexity-entropy causality plane: A useful approach to quantify the stock market inefficiency," *Physica A: Statistical Mechanics and its Applications*, vol. 389, no. 9, pp. 1891 – 1901, 2010.

[50] L. Zunino, M. C. Soriano, I. Fischer, O. A. Rosso, and C. R. Mirasso, "Permutation-information-theory approach to unveil delay dynamics from time-series analysis," *Phys. Rev. E*, vol. 82, p. 046212, Oct 2010.

[51] M. Riedl, A. Müller, and N. Wessel, "Practical considerations of permutation entropy," *The European Physical Journal Special Topics*, vol. 222, no. 2, pp. 249–262, 2013.

[52] Y.-Q. L. G. P. Orlando, S. and R. Rosner, "Alfvénic fluctuations in fast and slow solar winds," *J. Geophys. Res.*, vol. 102, p. 2413924149.